NASA/TM-2002-211432

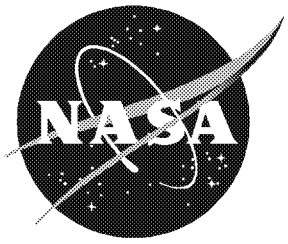

Aeroacoustic Experiments in the Langley Low-Turbulence Pressure Tunnel

Meelan M. Choudhari, David P. Lockard, Michele G. Macaraeg, Bart A. Singer, and Craig L. Streett
Langley Research Center, Hampton, Virginia

Guy R. Neubert, Robert W. Stoker, and James R. Underbrink
Boeing Commercial Aircraft, Seattle, Washington

Mert E. Berkman, Mehdi R. Khorrami, and Shelly S. Sadowski
High Technology Corporation, Hampton, Virginia

February 2002

The NASA STI Program Office . . . in Profile

Since its founding, NASA has been dedicated to the advancement of aeronautics and space science. The NASA Scientific and Technical Information (STI) Program Office plays a key part in helping NASA maintain this important role.

The NASA STI Program Office is operated by Langley Research Center, the lead center for NASA's scientific and technical information. The NASA STI Program Office provides access to the NASA STI Database, the largest collection of aeronautical and space science STI in the world. The Program Office is also NASA's institutional mechanism for disseminating the results of its research and development activities. These results are published by NASA in the NASA STI Report Series, which includes the following report types:

- TECHNICAL PUBLICATION. Reports of completed research or a major significant phase of research that present the results of NASA programs and include extensive data or theoretical analysis. Includes compilations of significant scientific and technical data and information deemed to be of continuing reference value. NASA counterpart of peer-reviewed formal professional papers, but having less stringent limitations on manuscript length and extent of graphic presentations.

- TECHNICAL MEMORANDUM. Scientific and technical findings that are preliminary or of specialized interest, e.g., quick release reports, working papers, and bibliographies that contain minimal annotation. Does not contain extensive analysis.

- CONTRACTOR REPORT. Scientific and technical findings by NASA-sponsored contractors and grantees.

- CONFERENCE PUBLICATION. Collected papers from scientific and technical conferences, symposia, seminars, or other meetings sponsored or co-sponsored by NASA.

- SPECIAL PUBLICATION. Scientific, technical, or historical information from NASA programs, projects, and missions, often concerned with subjects having substantial public interest.

- TECHNICAL TRANSLATION. English-language translations of foreign scientific and technical material pertinent to NASA's mission.

Specialized services that complement the STI Program Office's diverse offerings include creating custom thesauri, building customized databases, organizing and publishing research results . . . even providing videos.

For more information about the NASA STI Program Office, see the following:

- Access the NASA STI Program Home Page at ***http://www.sti.nasa.gov***

- Email your question via the Internet to help@sti.nasa.gov

- Fax your question to the NASA STI Help Desk at (301) 621-0134

- Telephone the NASA STI Help Desk at (301) 621-0390

- Write to:
  NASA STI Help Desk
  NASA Center for AeroSpace Information
  7121 Standard Drive
  Hanover, MD 21076-1320

NASA/TM-2002-211432

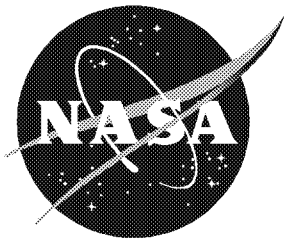

Aeroacoustic Experiments in the Langley Low-Turbulence Pressure Tunnel

Meelan M. Choudhari, David P. Lockard, Michele G. Macaraeg, Bart A. Singer, and Craig L. Streett
Langley Research Center, Hampton, Virginia

Guy R. Neubert, Robert W. Stoker, and James R. Underbrink
Boeing Commercial Aircraft, Seattle, Washington

Mert E. Berkman, Mehdi R. Khorrami, and Shelly S. Sadowski
High Technology Corporation, Hampton, Virginia

National Aeronautics and
Space Administration

Langley Research Center
Hampton, Virginia 23681-2199

February 2002

Acknowledgments

Many individuals contributed to various aspects of this work. The authors especially would like to thank the crews at the Langley Low-Turbulence Pressure Tunnel for making this work possible.

Available from:

NASA Center for AeroSpace Information (CASI)
7121 Standard Drive
Hanover, MD 21076-1320
(301) 621-0390

National Technical Information Service (NTIS)
5285 Port Royal Road
Springfield, VA 22161-2171
(703) 605-6000

Contents

Nomenclature

c	speed of sound
$\overline{c}$	cruise-wing chord
C_p	pressure coefficient
f	frequency
M	Mach number
Re	Reynolds number based on $\overline{c}$
SPL	sound pressure level
x	streamwise distance along wing
α	angle of attack of configuration
δ_f	flap deflection
δ_s	slat deflection downward

Abstract

A phased microphone array was used in the Langley Low-Turbulence Pressure Tunnel to obtain the radiated acoustic field from high-lift wing configurations that included a slat and a part-span flap. The data included noise localization maps and acoustic spectra.

1. Introduction

Airframe-generated noise is an important component of the total noise radiated from commercial aircraft, especially during the approach. Recent studies by Davy and Remy (ref. 1) on a scale model of an Airbus aircraft indicate that the high-lift devices and landing gear are the main sources of airframe noise when the aircraft is configured for approach. Earlier tests on a model of a McDonnell Douglas DC-10 aircraft also identified the high-lift system as an important airframe noise source (ref. 2). Dobrzynski et al. (ref. 3) performed full-scale experimental studies in an open-jet wind tunnel on a portion of a wing equipped with a high-lift system. They found that both the leading-edge slat and the side edge of the trailing flap contributed significantly to airframe noise.

An extensive experimental and computational effort to study the various mechanisms associated with airframe-generated noise continues at NASA Langley Research Center (ref. 4), including tests performed in the NASA Langley Quiet Flow Facility (QFF) (refs. 5-7). Many aspects of the work are described elsewhere (refs.8-10); this report documents the experimental conditions and the salient results.

Section 2 discusses the experimental facility, the model geometries, and the instrumentation used. Section 3 summarizes the results and important conclusions from the various tests.

2. Experimental Details

This report documents three wind tunnel entries. The first entry, in August 1997, focused on noise emanating from the flap side edge. This wind tunnel entry is logged as Flap-Edge Noise Test 403. The second entry, in April 1998, explored some noise-reduction technologies for flap-side-edge noise and then examined slat noise. The respective portions of the tests are logged as Flap-Edge Noise II Test 409 and Slat Noise Test 410. The third entry, in June 1999, tested some noise-reduction techniques for slat noise and then studied landing-gear noise. These studies are logged as Acoustics-Flap Noise Test 420 and Acoustics-Landing Gear Test 421, respectively. Details of the landing-gear test are not discussed here.

2.1. Experimental Facility

The tests involved a series of aeroacoustic experiments performed in the Langley Low-Turbulence Pressure Tunnel (LTPT). The LTPT is a closed-loop wind tunnel that can operate at pressures up to 10 atm, thereby providing the capability to test at variable Reynolds numbers without changing the Mach number. This capability, critical to these tests, enabled clear determination of which effects were Reynolds number related and which could reasonably be expected to exist in flight. A detailed description of the tunnel is given by McGhee, Beasley, and Foster (ref. 11). Some details pertinent to these tests are summarized below.

Unfortunately, the wind tunnel is not well suited for aeroacoustic tests. The tunnel walls are all hard and the test section is not large; its dimensions are 3 ft wide, 7.5 ft high, and 7.5 ft long (0.98 m × 2.46 m × 2.46 m). The tunnel has a passive boundary layer control system for venting sidewall

boundary layers through porous endplates, but aeroacoustic concerns led to the use of solid endplates. The tunnel temperature was controlled by tunnel cooling vanes, but automatic control of tunnel pressurization was disabled to avoid noise introduced by control vanes. Another aeroacoustic concern was the model support arc sector that extends from the tunnel floor to the ceiling at the downstream end of the test section. The arc sector is designed to support instrumentation for measuring details of the model wake. Left untreated, openings in the arc sector (such as screw holes and recesses for mounting equipment) were a major source of noise. Simply taping the openings was insufficient; the high operational pressures often burst the tape. Ultimately a metal plate was fabricated to cover several major openings, all remaining openings in the arc sector were caulked with acrylic caulk.

The target Reynolds numbers based on the model mean chord in the cruise configuration were 3.6, 7.2, 14.4, and 19.2×10^6. The target Mach numbers were 0.125, 0.2, and 0.3. Not all entries were run at all Reynolds and Mach numbers. Because strong Reynolds number effects were observed only for the lowest Reynolds number, most of the runs used a Reynolds number (Re) of 7.2×10^6 or greater. The Mach number (M) of 0.2 was selected as the baseline Mach number for these tests; the other Mach numbers were used primarily to determine scaling laws.

2.2. Airframe Model

The two-dimensional (2D) NASA Energy Efficient Transport (EET) wing described by Morgan (ref. 6) served as the basic model for the tests. In the cruise configuration, the wing has a chord $\bar{c}$ of 21.65 in. (55 cm); this is the chord with which lengths will be nondimensionalized. In the 1998 and 1999 tests, the same leading-edge slat was used. This slat has been described by Lin and Dominik (ref. 13). No leading-edge slat was used in the 1997 test. Two flap configurations were used in the tests. In both the 1997 and 1998 tests, a part-span trailing flap was used. The part-span flap had a span of 19 in. (48.26 cm) and a 6.5 in. (16.5 cm) chord (30 percent of chord). For the 1999 test, a full-span trailing flap was desired. Unfortunately, a full-span version of the part-span flap previously tested was not available. Rather than build an entirely new full-span flap, the full-span flap of Lin and Dominik (ref. 13) was used. This flap was also a 30-percent chord flap, but its contour differed from that used in the previous tests.

Schematics of the high-lift configurations used in the 1997 and 1998 tests are shown in figures 1(a) and (b), respectively. Gaps, overlaps, and deflection angles were all defined consistent with figure 6 of Lin and Dominik (ref. 13). The slat and flap overhangs were set using blocks machined to match the main element contour, whereas the gaps were set by rearranging spacers at the feet of the support brackets. Modifications to the basic wing will be described briefly in the noise-reduction sections below.

In the tests that focused on flap noise (the 1997 and the first part of the 1998 tests), the model was mounted in the wind tunnel with the suction side of the wing facing the wind tunnel ceiling. For the other tests the model was inverted so that the pressure side faced the wind tunnel ceiling. These arrangements were selected to center the acoustic array (described below) over the region of interest in the particular tests. For the slat portion (i.e., the second part) of the 1998 test, the model was also moved downstream approximately 29 in. (73.66 cm) to position the slat more nearly under the acoustic array. The translation required the construction of a manual turntable and mounting system. For the 1999 tests, the standard turntable and mounting system was used.

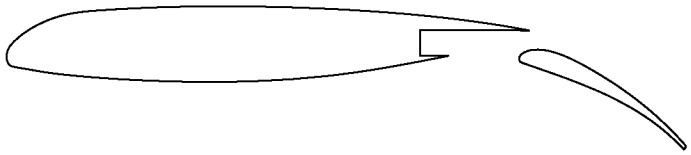

(a) Configuration for 1997 test and first part of 1998 test.

(b) Configuration for second part of 1998 test.

Figure 1. High-lift wing section. Slotted flap shown with flap deflection $\delta_f = 30°$. Slat shown with slat deflection $\delta_s = 30°$.

2.3. Instrumentation

Various types of measurements were taken during these tests. Pressure-sensitive paint was used during the 1997 entry to determine flap-side-edge vortex paths. This technique was not used during later wind tunnel entries. Surface pressure measurements were taken for portions of all three entries. Extensive phased microphone array data were taken during all three entries. Additional aerodynamic data were taken during aerodynamic portions of the 1997 and 1998 entries and will be reported elsewhere.

2.3.1. Pressure-Sensitive Paint

Pressure-sensitive paint (PSP) was used to help determine vortex trajectories associated with the flap side edge. The paint changes color in response to the local static pressure. Vortices near a solid surface leave a low-pressure footprint on the surface. A team from what was then McDonnell Douglas Corporation applied the paint, took the photographs, processed the data, and plotted the mean pressure fields on the flap surfaces. Data were obtained from cameras directed to the top of the flap (camera 3) and the side edge of the flap (camera 4). The processed data on the flap top and side surfaces are in digital format and can be viewed from a variety of angles. A more detailed analysis of the data is presented in the section entitled "Mean Flow."

2.3.2. Surface Pressure Ports

The models included surface pressure ports for obtaining static pressure at discrete locations on the models.

2.3.3. Unsteady Surface Pressure

Several of the models were outfitted with fluctuating pressure transducers for obtaining unsteady pressure measurements on the wing elements. Most of the unsteady pressure data acquisition was performed with a mix of equipment and staff from High Technology Corporation and The Boeing Company. During the 1997 test, the signals from the unsteady pressure transducers were low-passed filtered at 40 kHz. During the 1998 test, the unsteady pressure transducer data were reliable to a frequency of about 70 kHz.

2.3.4. Phased Microphone Array

The microphone array and processing software were supplied by The Boeing Company. Underbrink and Dougherty (ref. 14) and Dougherty (ref. 15) describe the use of logarithmic spirals in phased microphone arrays. This spiraled array improves the signal-to-noise ratio available compared to conventional microphone array configurations. The improved signal-to-noise ratio allows for the acquisition of acoustic data in hard-wall tunnels. Mosher (ref. 16) and Mosher et al. (ref. 17) address some additional issues that arise when using arrays in hard-wall wind tunnels.

The microphone array was installed in the ceiling of the wind tunnel test section by covering three removable ceiling sections with a single 1/2 in. thick plate faired at the upstream and downstream ends. Microphones were placed in the regions where the ceiling sections were removed. The positions of the ceiling sections are indicated in figure 2. The large array employed 52 microphones embedded in the plate with Boeing custom-designed flush-mount microphone adapters. In the 1997 entry, Brüel and Kjær (B&K) 4136 microphones were connected to B&K flex-necks to adapt half-inch Larson Davis preamplifiers (model number 900B) to the quarter-inch microphones. Larson Davis 12-channel power supplies (model number 2212) were located inside the pressure chamber (but outside of the test section) and the analog signals were brought out of the pressure chamber by means of connector patch panels that are part of the tunnel wiring infrastructure. Data provided by B&K indicate that the B&K 4136 microphones experience a sensitivity reduction of 25 dB at 50 kHz and 6 atm. as compared to 1 atm.

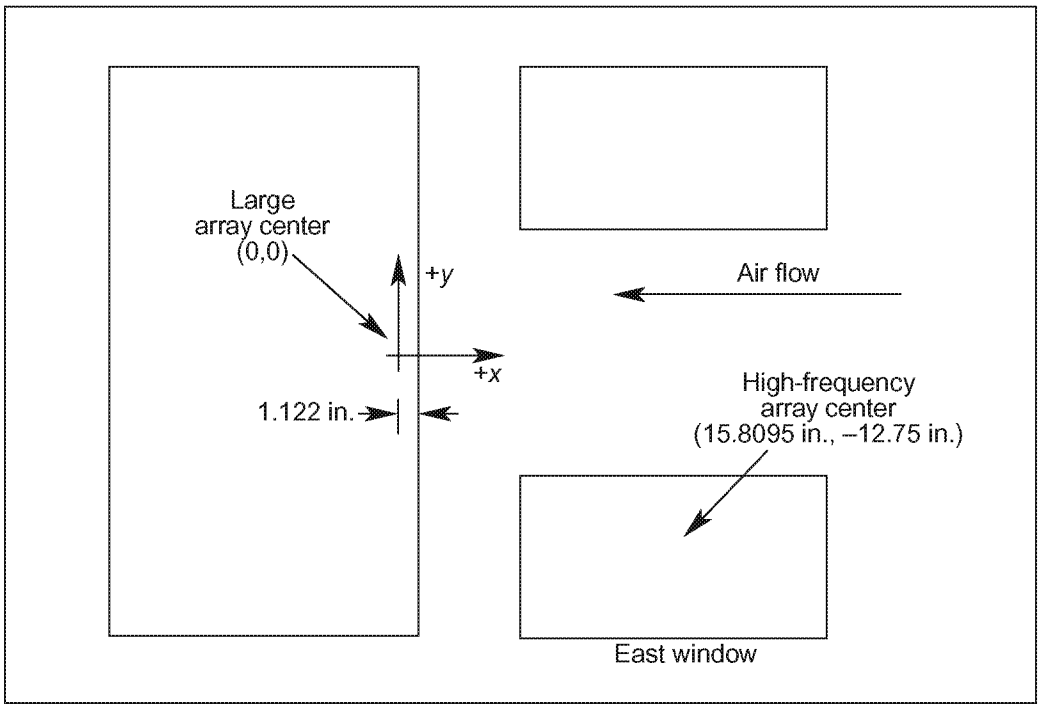

Figure 2. Schematic of plate and removed ceiling sections in LTPT. View is from above test section; array centers are centroids of microphones actually used in corresponding arrays.

Subsequent tests used B&K 4136 WB1437 microphones, which have a substantial sensitivity improvement at high frequencies under pressurized conditions. The maximum loss in sensitivity with the new microphones was about 15 dB at approximately 40 kHz. The use of the new microphones improved the dynamic range of the measurements. The 1999 test had an additional equipment upgrade with the use of B&K preamplifiers (model number 2670/WH3188) and Boeing-built 16-channel power supplies.

In all tests, data were acquired as time series with Hewlett Packard HP-3565 data acquisition hardware. The system consisted of an HP-35654A control module, an HP-35653A source module, two HP-35659A SCSI (small computer system interface) disk controller modules, and up to 60 HP-35652B input modules with 102.4 kHz data bandwidth. The input modules contained all the necessary signal conditioning for quality digital data acquisition, including analog antialiasing filters, 16 bit A/D (analog to digital) converters (dynamic range of 75 dB). The converters have ranging capability that enables dynamic range optimization when digitizing the data. Using Boeing custom data acquisition software, digital data were streamed in real time to two SCSI disk drives of 2 Gb each and successively uploaded to the host computer (an HP-9000/385 workstation). On the host computer they were written to binary files as digitized (raw integer) values, along with information to convert the data to volts.

The design of the large-aperture array used in all three tests is best understood by examination of figure 3. An odd number of microphone locations (13) were equally spaced around a series of 10 concentric circles. Intersections of the circles with a logarithmic spiral (locations marked with solid circles) were chosen so that each microphone location would occupy an equal aperture area on the array panel (except for the innermost circle, which was chosen independently). A complete array would include microphones at all the indicated locations. However, limited access in the wind tunnel restricted the microphone positions to those that comfortably fit in the removed ceiling sections, which are represented by the three rectangular regions.

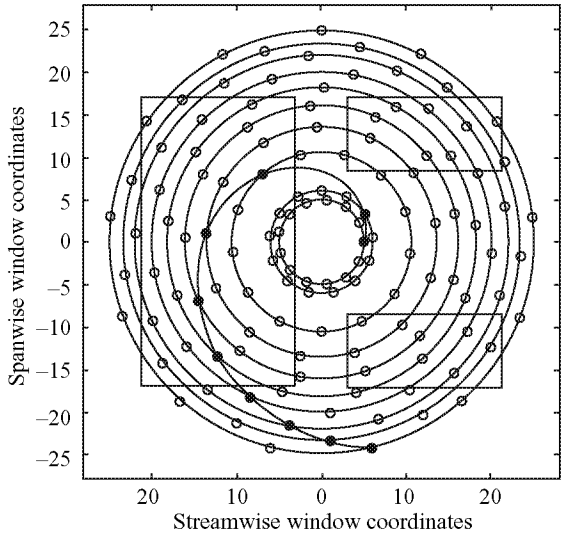

Figure 3. Schematic of microphone array. Open circles show desired locations of microphones; rectangular boxes show regions in which microphones were actually included; solid circles show intersection of logarithmic spiral with concentric circles.

The array was initially designed to work well up to a frequency of 40 kHz, but tests indicated that the strongest sidelobe at 80 kHz was not significantly stronger than that at 40 kHz. For most frequencies, the worst case sidelobe in a plane parallel to the array, at a distance equal to the distance of the model from the array, was approximately 8 dB down from the peak. However, designing an array on a panel where relatively large regions are not instrumented yielded an undesirable outcome, as described below.

In the past, until and including this work, the array design process involved the evaluation of array resolution and sidelobe characteristics on a planar surface near the region of interest for the test. Worst case sidelobes were determined at many frequencies on a planar surface parallel to the array surface at the same distance from the array as the model would be during the test. This process did not detect large out-of-plane sidelobes that were later discovered for this array. Fortuitously, the out-of-plane sidelobes were above-and-aft and below-and-forward of a source near the flap edge, and therefore did not interfere with flap-side-edge measurements.

In designing an array, another important issue should be considered. Volumetric beamforming shows that isosurfaces of constant noise level are ellipsoids with major axes oriented on a line from the source to the phase center of the array. This orientation means that the worst resolution (ability to separate closely spaced sources) is along this major axis. In cases in which multiple noise sources need to be considered, care should be taken to ensure that the sources are not collinear with the phase center of the array. Such collinearity would make distinguishing the different noise sources very difficult. For instance, this situation could arise if a landing gear were mounted on the wing and the array center, the wheels of the landing gear, and the slat gap were all collinear.

The 1999 wind tunnel experiment also included a 60-microphone small-aperture array, located in the east window plate of the wind tunnel (see fig. 2). This array was designed to work well up to a frequency of 80 kHz, and therefore is sometimes referred to as the high-frequency array. Each concentric circle of the array included 11 equally spaced microphones. Their relative positions were chosen by using a procedure similar to that used for the large-aperture array. The panel's layout of microphones is shown in figure 4. In the figure, the asterisks mark the location of microphones associated with the large-aperture

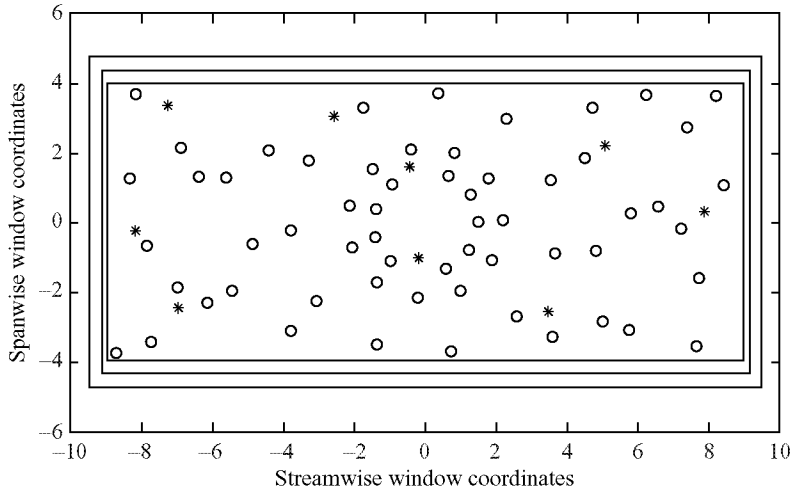

Figure 4. Schematic of microphones mounted in east window plate. Circles show locations of microphones for small-aperture array; asterisks show locations of microphones used in large-aperture array.

array. Where these large-aperture microphone locations were too close for mounting purposes to the desired location of a microphone for the small-aperture array, the small-aperture microphone was excluded. The configuration of the array was chosen from analytical and empirical data regarding the slat noise source. All microphones in the small-aperture array were intended to be within the main lobe of the slat noise source, where the main lobe was obtained from Singer, Lockard, and Brentner (ref. 8).

Calibrations were performed across the frequency range of interest with multiple speaker sources, including a low-frequency pipe speaker, a supertweeter, and an ionophone. The speakers were carefully positioned and the positions documented. The known geometry enabled determining the as-installed channel-to-channel phase and amplitude differences between the end-to-end measurement system channels. A spectrum from a reference microphone (a central microphone in the array) was captured for use in calibrating the array level. Pressure-response data were applied to the reference microphone to account for microphone sensitivity variations under pressurized conditions. In the 1999 test, a sonic digitizer was used for the first time to determine test geometry. This method provided more accurate determination of test geometry than the previous plumb bob and tape measure methods. However, the tight confines of the LTPT test section made using the sonic digitizer array difficult.

Processed acoustic array data provided "source localization maps" for each frequency processed. Poor spatial resolution in the direction normal to the array undermined associating a noise source with either the upper or lower side of the flap based only on a single figure. In practice, viewing multiple planes of such data is useful and often gives hints that strongly suggest one source over the other, but precise localization in the normal direction is not yet possible. However, the acoustic array had good spatial resolution in planes parallel to the array, so the localization maps were useful for localizing concentrated uncorrelated sources in the contour plane. The acoustic array postprocessing was not suited for localizing spatially extended sources (like conventional trailing-edge noise) nor sources that were correlated. For uncorrelated sources, sidelobes typically appeared about 8 dB below the peak amplitude. For distributed sources, the sidelobes could appear at amplitudes much closer to the peak.

More difficulties were encountered when data at different frequencies were to be compared. Most often, spatially integrated spectra were chosen for study. The integrated spectra were 1/12-octave in frequency and had been integrated over the spatial domain. Grid points with noise amplitudes more than 8 dB down from the peak were not included in the integration. The exclusion of these points from the integration was intended to avoid integrating the sidelobe contributions.

Although this procedure is generally believed to provide useful information, on occasion it has the potential to be deceiving. In particular, at a given frequency, consider a baseline case in which noise emanates at about the same amplitude from a large portion of the spatial domain. All of the grid points will be included in the integrated result for this baseline case. If some modification to the baseline configuration were to introduce a new high-amplitude source that was highly localized in the domain and more than 8 dB stronger than the background noise that previously existed, most of the grid points that previously contributed to the integrated results would be discounted in the new integration because their amplitude would be more than 8 dB down from the peak. Depending upon the details, this phenomenon could result in the louder noise case actually integrating to a lower value than the baseline case. This situation was avoided in most cases by considering both peak and integrated results during data reduction and evaluation.

In spite of these difficulties, the acoustic arrays provide valuable information for unraveling the physics and evaluating various noise-reduction techniques.

3. Results

3.1. Flap Side Edge

Noise generated near the side of the flap is related to the unsteady flow associated with the side-edge vortices. Therefore, considerable effort was expended in understanding the details of the vortices in the vicinity of the flap side. Both computational and experimental efforts focused towards understanding this flow are reported by Berkman et al. (ref. 9). Section 3.1.1 describes the mean flow. In section 3.1.2, experimentally obtained surface pressure information is supplemented with knowledge of the flow obtained from numerical simulations. Section 3.1.3 describes key features of the acoustic field. Finally, section 3.1.4 concludes with a review of the performance of noise-reduction techniques for the flap side edge.

3.1.1. Mean Flow

A rendition of the main element and the flap is shown in figure 5. The dashed line is approximately 1.0 in. (2.54 cm) inboard of the flap side edge and indicates the approximate location of the line of pressure taps used to obtain the pressure distribution over the main element and the flap as illustrated in figure 6. The second suction peak on the flap is caused by strong suction of the vortex. Pressure distributions farther from the flap side edge do not show the second peak. The main element used was not the cruise-configuration main element, but the high-lift configuration without the leading-edge slat.

Essentially continuous pressure distributions from the PSP measurements are shown in figure 7. The pressure distributions confirm that a dual vortex system exists near the flap side edge. In the current tests, the stronger vortex forms on the flap top surface. This result differs from observations made with a different configuration that was tested in the NASA Langley Quiet Flow Facility (QFF) and the Ames 7- by 10-Foot Subsonic Wind Tunnel (refs. 18–20). As shown in figure 8, five-hole probe measurements from the QFF show that the stronger vortex in those experiments developed on the flap side edge. The flap side-edge vortex then merged with the flap top surface vortex (ref. 18). However, the general trajectories of the vortices are similar. In the current experiments, the low-pressure region near the side edge of the flap top surface in figure 7 reveals that the flap-top vortex moves slightly inboard as it moves downstream. The weaker vortex forms on the flap side edge close to the bottom corner where the boundary layer on the flap separates. It grows in strength in the downstream direction and eventually migrates onto the flap-top surface, where it merges with the flap-top vortex.

The delayed growth of the flap-side-edge vortex relative to that in the QFF experiments is related to the extensive side-lap region for this wing. With reference to figures 9a and 9b, the side-lap region is the space near the flap side edge between the flap and the aft portion of the wing on the portion without a flap. The side-lap region extends over approximately 40 percent of the flap chord.

Figure 10, which is taken from figure 6 of Berkman et al. (ref. 9), shows a cross-stream plane of streamwise vorticity contours from a Reynolds averaged Navier-Stokes calculation of the flow. The view in the figure is towards the upstream direction. The presence of the side lap produces a high-speed flat jet of fluid that results in a strong shear layer that separates from the main element. This shear layer quickly rolls up into a main-element vortex with a sign opposite to that of the flap-side-edge and flap-top vortices. The presence of the main-element vortex appears to flatten the flap-top vortex and delay the merging of the flap-side-edge vortex with the flap-top vortex relative to what was observed in the experiments performed in the QFF. The configuration used in the QFF had a smaller side-lap region.

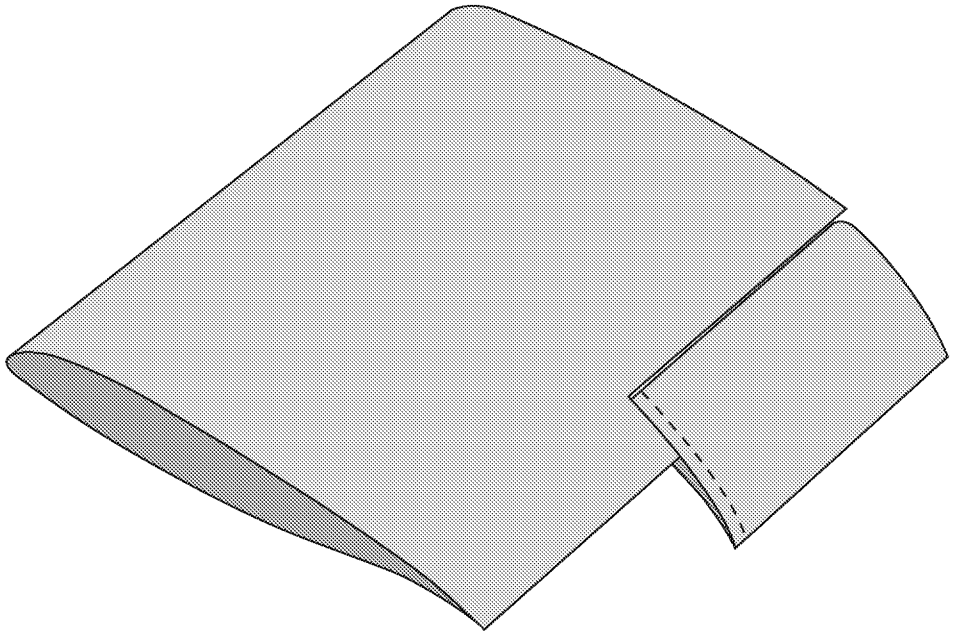

Figure 5. Three-dimensional view of main element and flap. Dashed line on flap shows approximate location of line of pressure taps.

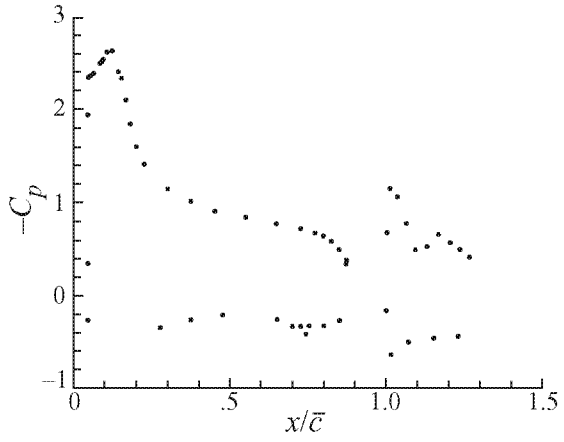

Figure 6. Chordwise pressure distribution over wing model with single slotted flap. Spanwise location is approximately 1 in. inboard of flap edge; $\alpha = 5°$; $\delta_f = 20°$; Re = 7.2×10^6; $M = 0.2$.

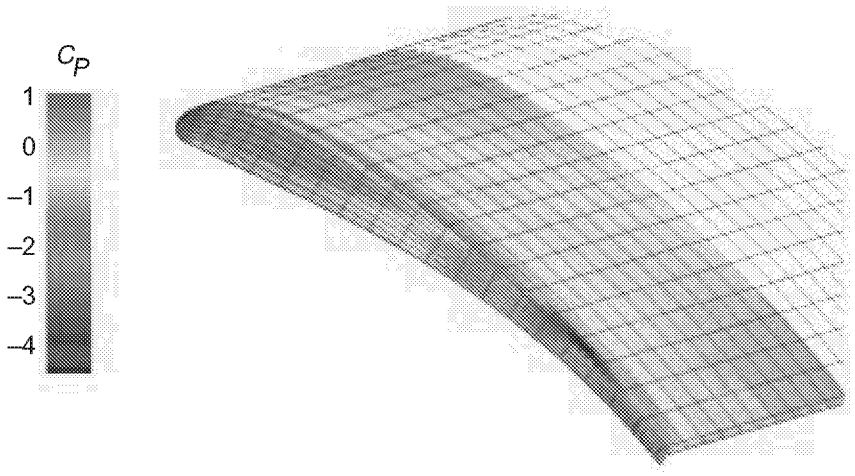

Figure 7. Pressure-sensitive paint measurements. $\alpha = 5°$; $\delta_f = 20°$; Re = 7.2×10^6; $M = 0.2$.

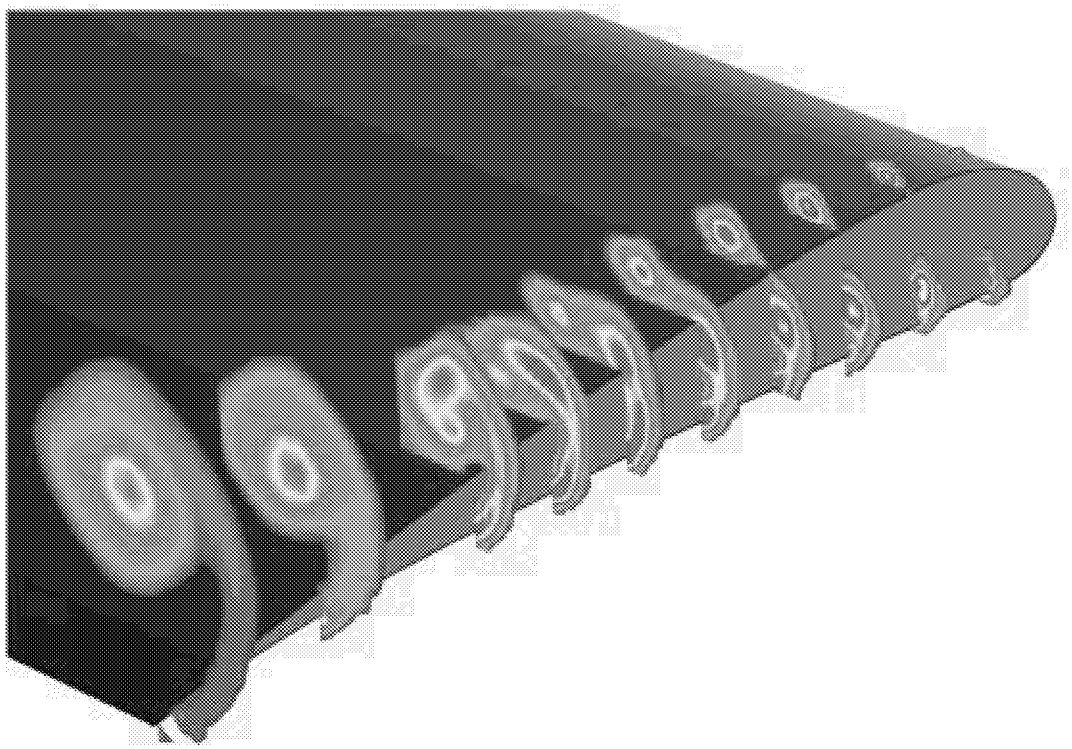

Figure 8. Vorticity contours from 5-hole pressure probe measurements in the QFF.

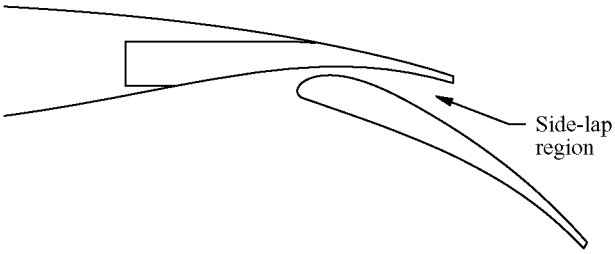

(a) View from side.

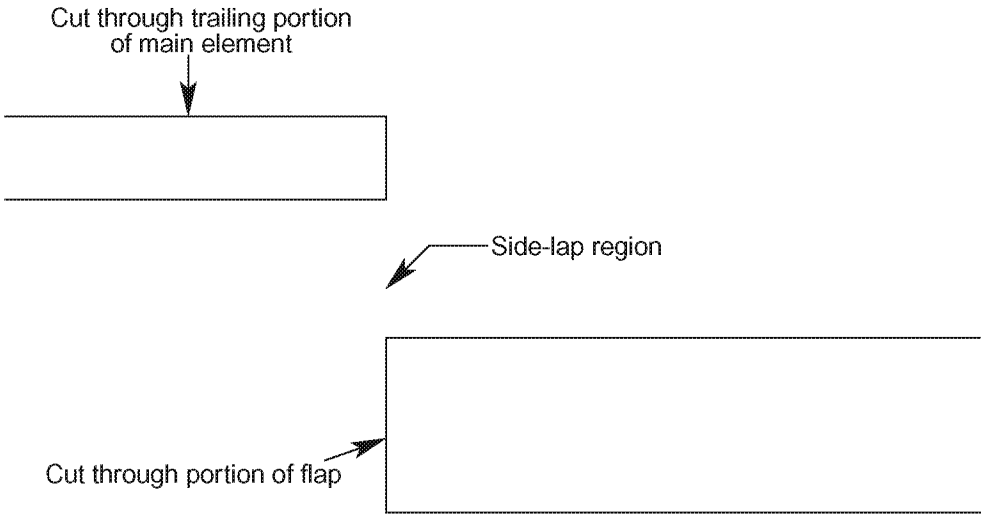

(b) View from downstream.

Figure 9. Schematic of side-lap region between flap and aft portion of unflapped side of wing

As expected, all vortices are stronger with $\delta_f = 30°$ than with $\delta_f = 20°$. With $\delta_f = 20°$, only very mild strengthening of the vortices occurs with increases in the Reynolds number. The Reynolds number effect appears to be slightly stronger, but still rather weak, with $\delta_f = 30°$. Whether these changes with Reynolds number are significant is not clear.

3.1.2. Unsteady Surface Pressures

The unsteady pressure transducer distribution used on the flap in the 1997 test is illustrated in figure 11. In figure 11 the transducers are indicated by the rectangles with a darkened square at one end. The darkened squares indicate the active sensing region of each transducer. The transducers on the flap suction surface that are referenced later are labeled A-C. The two transducers on the flap side edge are numbered 1 and 2. Autospectra from these transducers are shown in figure 12. These spectra show that transducer 1 has two low-frequency peaks, suggesting that coherent oscillations of the flap-side-edge vortex are present at its location. In contrast, the spectrum of transducer 2 is featureless, thereby suggesting that the flap-side-edge vortex has already moved to the suction surface.

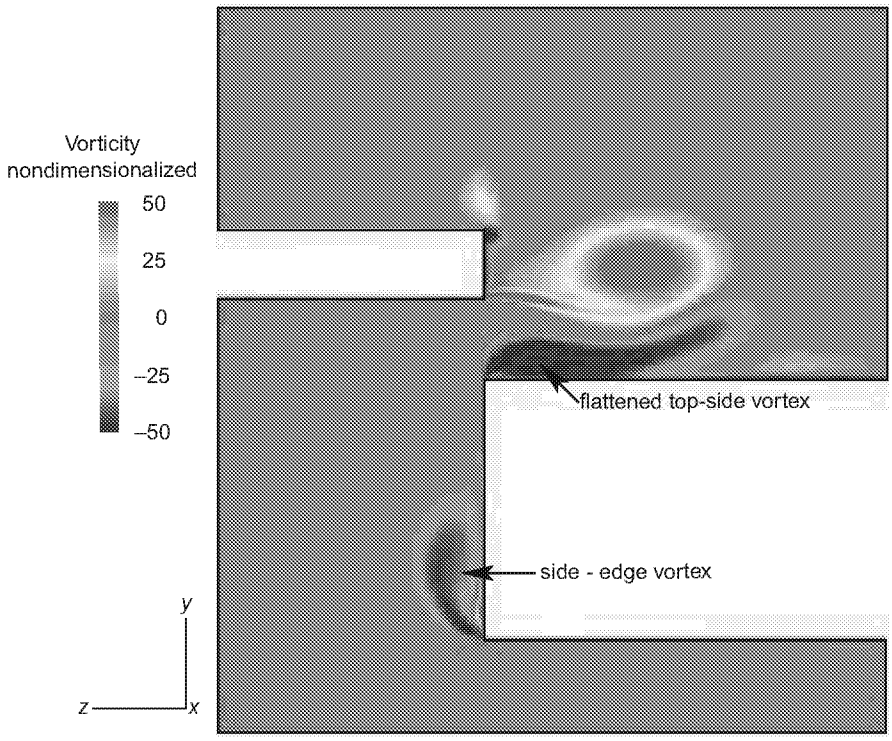

Figure 10. Color contours of streamwise vorticity from Reynolds averaged Navier-Stokes calculation. $\alpha = 5°$; $\delta_f = 20°$; Re = 7.2×10^6; $M = 0.2$; view is looking upstream; plane is located at $x/\overline{c} = 0.94$; trailing portion of main element is on left side; flap is on right side.

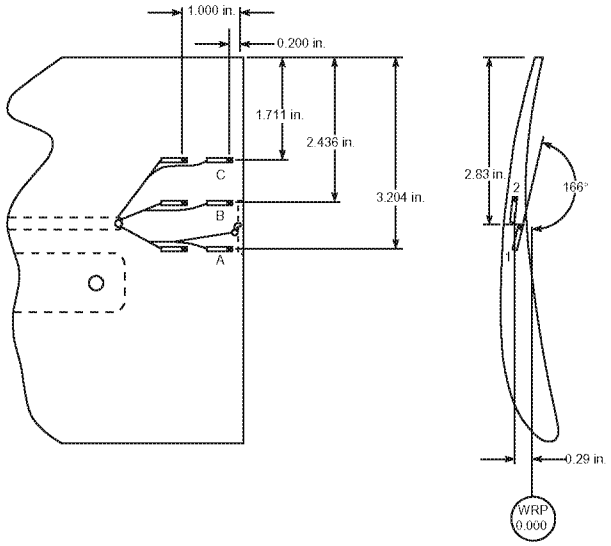

Figure 11. Schematic of unsteady pressure transducer distribution on flap side edge in LTPT tests. WRP is wing reference plane. Transducers on the flap suction surface that are referenced later are labeled A-C. Transducers on the flap side edge are labeled 1 and 2. Darkened squares are the active sensing regions.

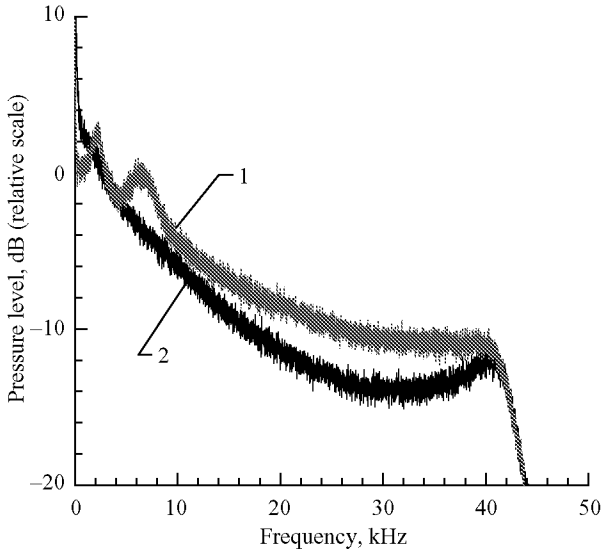

Figure 12. Autospectra from transducers 1 and 2. $\delta_f = 30°$; Re = 7.2×10^6; $M = 0.2$.

Transducers A, B, and C are near the flap side edge on the suction surface (see fig. 11). As shown in figure 13, the maximum amplitude signal is observed at transducer C. At this location, the flap-side-edge vortex has probably merged with the flap-top vortex. The spectrum of transducer C is the pressure spectrum of the turbulence in the merged vortex system. Figure 14 shows the coherence between transducers B and C. The relatively strong coherence in the frequency range of 1500 to 4000 Hz suggests that the same large scale flow structures are responsible for 10 to 30 percent of the pressure oscillations at both locations.

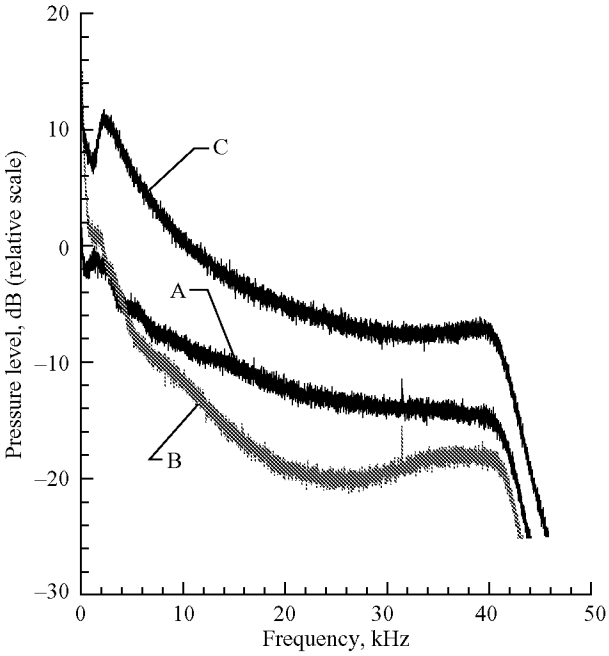

Figure 13. Autospectra from transducers A, B, and C. $\delta_f = 30°$; Re = 7.2×10^6; $M = 0.2$.

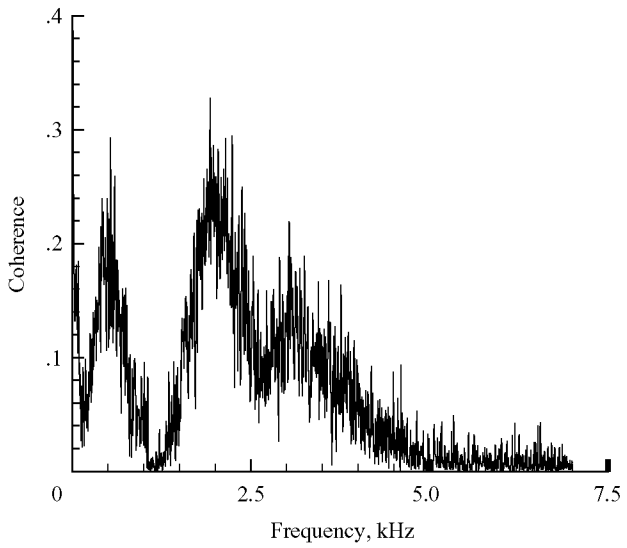

Figure 14. Coherence between transducers B and C. $\delta_f = 30°$; Re = 7.2×10^6; $M = 0.2$.

3.1.3. Acoustics

Acoustic measurements of noise originating at the flap side edge are consistent with previously proposed ideas of instabilities in the turbulent shear layer at the side edge (refs. 21–23). The noise generated at the flap side edge is most conveniently modeled as four sources that manifest themselves in the frequency ranges illustrated schematically in figure 15. The integrated 1/12-octave sound pressure level (SPL) on the vertical scale represents the 1/12-octave SPL integrated over a volume in the vicinity of the flap side edge. The localization maps shown in figures 17–20 include a rectangular frame that indicates the extent of a slice of the integration volume. The full integration volume includes similar slices stacked in the direction normal to the slices shown. The acoustic sources are believed to be the results of instabilities in the turbulent shear layers.

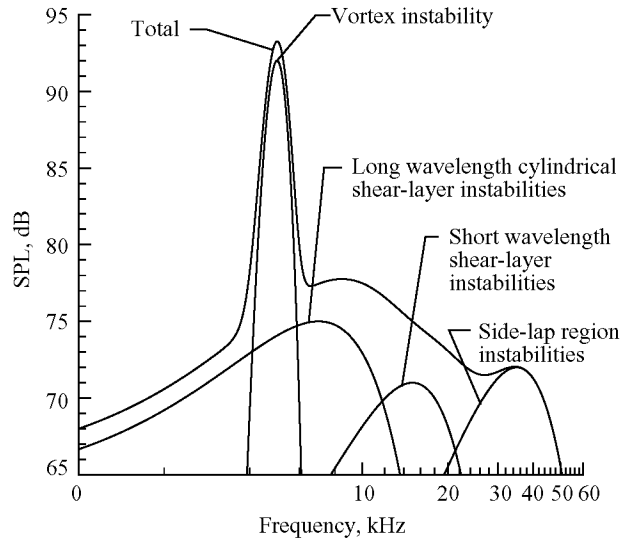

Figure 15. Schematic integrated 1/12-octave acoustic spectra of turbulent flap-side-edge noise sources.

An actual spectrum of the SPL integrated over the flap-side-edge region is shown in figure 16. The cutoff at 60 kHz is the result of a data management tradeoff and does not imply that no noise sources have frequencies that exceed 60 kHz. The strongest noise source in figure 16 is associated with a strong tone-like signal at slightly less than 5000 Hz.

Figures 17–20 show localization plots for run 61. The array centroid was approximately 1 m from the flap suction surface. All localization plots shown here illustrate contours from the local maximum to approximately 8 dB less than the maximum. Figure 17 shows a source localization plot of the noise at 4870 Hz.

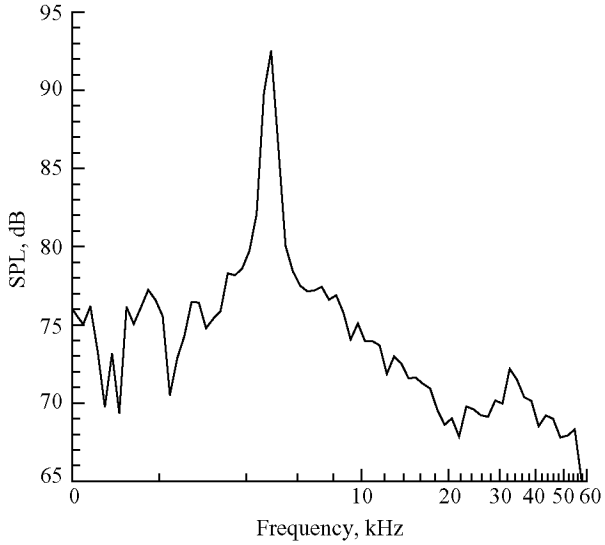

Figure 16. Integrated 1/12-octave acoustic spectrum for run 61 of 1998 test. $\delta_f = 30°$; Re = 7.2×10^6; $M = 0.2$.

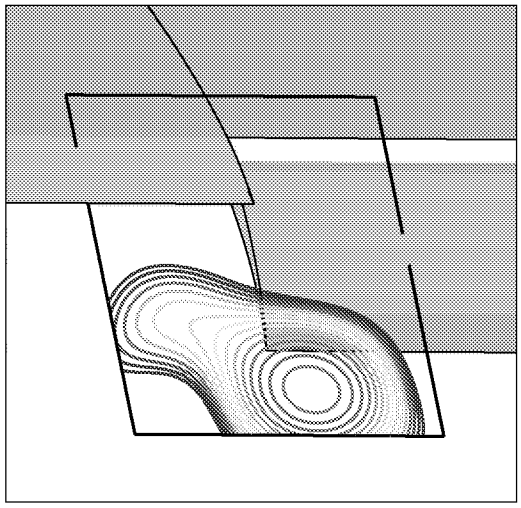

Figure 17. Localization plot for run 61 of 1998 test. f = 4870 Hz; $\delta_f = 30°$; Re = 7.2×10^6; M = 0.2; local 1/12-octave SPL peak is 92.5 dB.

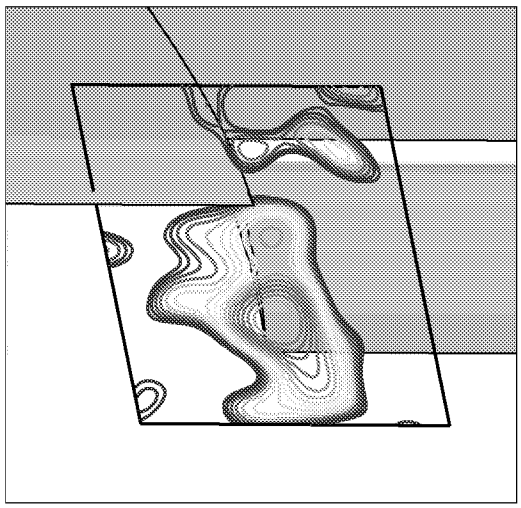

Figure 18. Localization plot for run 61 of 1998 test. $f = 9173$ Hz; $\delta_f = 30°$; Re = 7.2×10^6; $M = 0.2$; local 1/12-octave SPL peak is 70.0 dB.

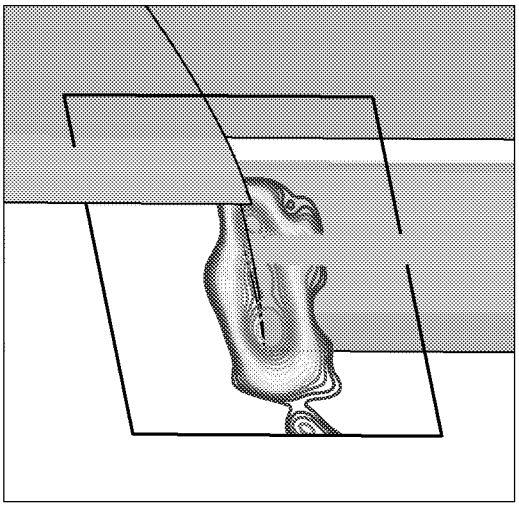

Figure 19. Localization plot for run 61 of 1998 test. $f = 16312$ Hz; $\delta_f = 30°$; Re = 7.2×10^6; $M = 0.2$; local 1/12-octave SPL peak is 62.8 dB.

The source localization plot in figure 17 shows that a strong source exists at the trailing corner of the flap side edge. This noise source is believed to be caused by interaction of unsteady flow structures in the merged flap-side-edge vortex with the flap trailing edge. The calculations of Streett (ref. 22) show the development of coherent, ringlike flow structures in the outer portion of the merged vortex. This noise source was effectively eliminated by the introduction of the noise weeder described below.

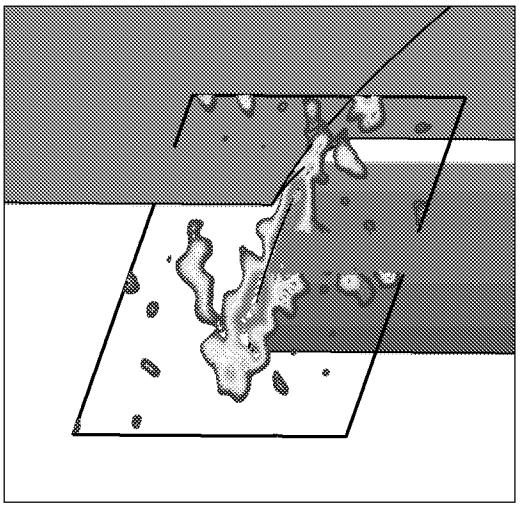

Figure 20. Localization plot for run 61 of 1998 test. View from pressure side of model. f = 36517 Hz; δ_f = 30°; Re = 7.2 × 10^6; M = 0.2; local 1/12-octave SPL peak is 54.9 dB.

As frequency increases, the dominant noise source tends to move upstream on the flap. Figures 18–20 show source localization maps at frequencies of 9173 Hz, 16312 Hz, and 36517 Hz, respectively. In the figures, the plane on which the contours are displayed intersects the flap suction surface. Because the array has poor resolution in the direction normal to the wall on which it is mounted, noise sources might appear to emanate from inside the solid model. However, in figure 18, no data are illustrated in the intersection region of the solid model and the plane of the localization map.

At all conditions, some noise radiates from the trailing-edge corner, but another important source appears on the side edge. The regions associated with flap-side-edge peaks in figures 18 and 19 are believed to result from instabilities in the turbulent shear layer at the flap side edge. These instabilities are consistent with the stability analyses of Khorrami and Singer (refs. 21 and 24) and the detailed numerical simulations of Streett (ref. 22). The calculations of Streett (ref. 22) clearly show the different nature of the instabilities in the high- and low-frequency ranges.

The source of the highest frequency noise at the flap side edge appears to be a vortex roll-up and the associated turbulent flow. This phenomenon results from the jet-like flow through the side-lap region between the pressure surface of the main element's trailing edge and the suction surface of the flap's leading edge. (Refer to figure 9 for the geometry.) The localization plot in figure 20 is shown from a slightly different angle than that of figures 17–19 to better reveal that the upstream noise source emanates from the side-lap region. This noise source is likely to be important only in high-lift devices with significant amounts of side lap.

3.1.4. Flap-Side-Edge Modifications

During the 1997 test, a variety of flap-side-edge modifications were tried, which primarily involved altering the shape of the flap side edge. Figure 21 shows the different flap edges used. The baseline flap edge (first from left in fig. 21) was flat, resulting in a sharp corner at both the lower and upper edges.

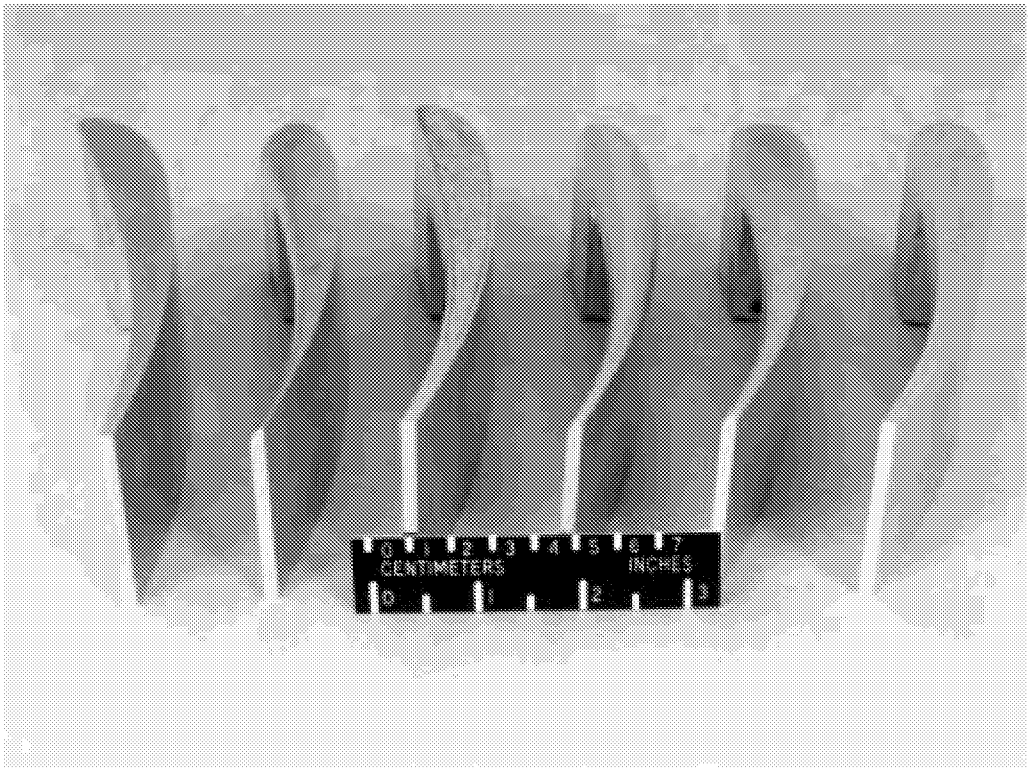

Figure 21. Different flap side edges used in 1997 tests, from left to right: baseline flap edge, half-round 1, flange filled with porous material, full-round, half-round 2, and half-round 3.

Three flap side edges with sharp corners at the upper edge, but with rounded lower edge, are denoted half-round 1, half-round 2, and half-round 3. The full-round was designed with the entire flap side edge rounded, so that neither the top nor bottom corners was sharp. The flange modification was a flat flapside-edge with a recessed center portion (not shown). A final modification (shown in fig. 21) involved the use of the flange with the recessed portion filled with a porous liner.

At low Reynolds numbers, the half-round configurations were noisier than the baseline, while the full-round configuration was slightly quieter than the baseline. With $Re = 14.4 \times 10^6$, where all of the modifications were tested, the half-round 1 modification remained somewhat noisier than the baseline, while the other modifications appeared to make no substantial change in acoustic radiation compared with the baseline edge. Figure 22 shows the spectra of the half-round modifications plotted together with the baseline case. Figure 23 shows the spectra for the remaining edge modifications and the baseline case. The small gaps in the data at about 4590 Hz and 23040 Hz are associated with the data processing algorithm used at that time.

With the knowledge gained from the 1997 test, two concepts for flap-edge modifications were tested in 1998. Based on the hypothesis that much of the noise at the side edge was associated with instabilities in the turbulent shear layer, a technique was developed to modify the shear layer to reduce the growth of these instabilities. The technique employed microtabs positioned near the flap side edge on the flap pressure surface. The microtabs are small trapezoidal devices that shed vortices from their corners and thereby increase the thickness of the resulting detached shear layer. A strip of microtabs attached to the pressure surface of the flap side edge is shown in figure 24. Detailed dimensions of typical microtabs

sized for the 1998 flap-side-edge noise reduction tests are shown in figure 25.

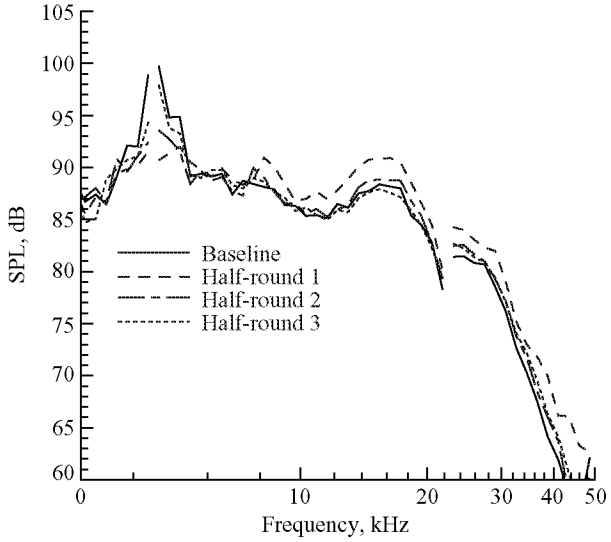

Figure 22. Integrated 1/12-octave acoustic spectra from 1998 test. $\delta_f = 30°$; Re = 14.4×10^6; $M = 0.2$.

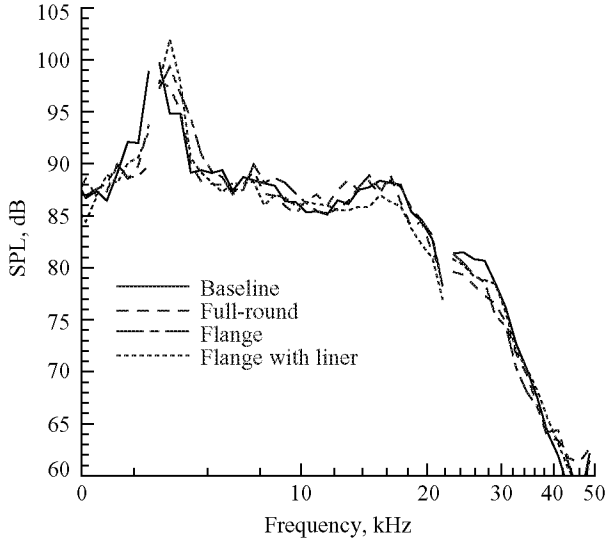

Figure 23. Integrated 1/12-octave acoustic spectra from 1998 test. $\delta_f = 30°$; Re = 14.4×10^6; $M = 0.2$.

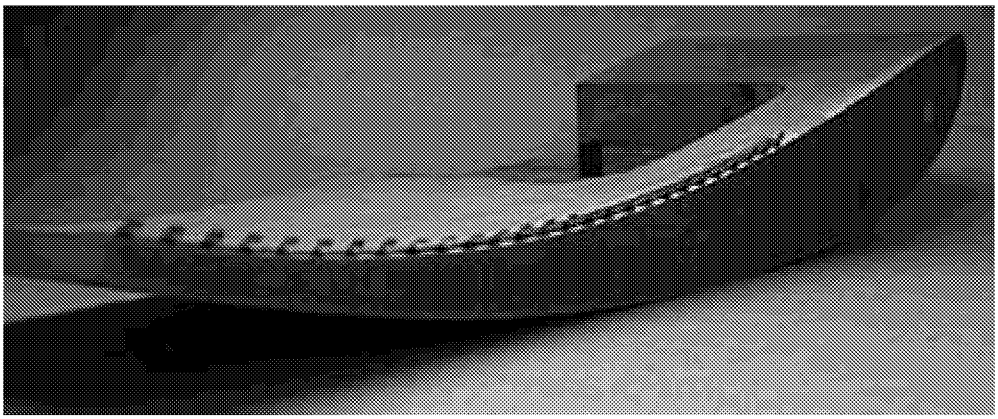

Figure 24. Microbtabs on flap side edge.

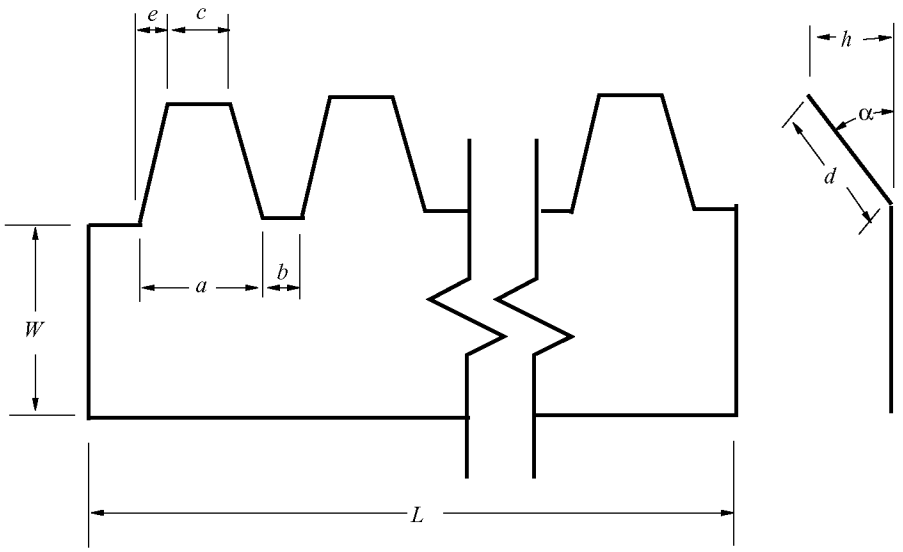

Figure 25. Schematic of typical microtab strip on flap side edge. For the LTPT experiments, $a = 0.075$ in., $b = 0.075$ in., $c = 0.051$ in., $d = 0.060$ in., $e = 0.012$ in., $h = 0.046$ in., $L = 4$ in., $W = 0.10$ in., $\alpha = 50°$.

The microtabs used in this application thicken the mixing region and decrease mean shear. The shear layers are therefore more stable because microtabs produce more mixing as a result of greater entrainment associated with small vortices generated by the microtabs.

Previous data indicate that a significant portion of the noise associated with the flap side edge radiates from the trailing-edge corner of the flap. The microtabs were designed to thicken the separated shear layer. Figure 26 shows results with and without the microtabs for runs with $\delta_f = 20°$. Noise was significantly reduced from approximately 7 kHz to 40 kHz. However, the microtabs apparently increase the noise between 40 and 50 kHz, probably by adding small-scale fluctuations to the flow. Details associated with microtab sizing and placement need to be explored more carefully to make this modification viable. Tests with the same placement of the microtabs and $\delta_f = 30°$ showed essentially no

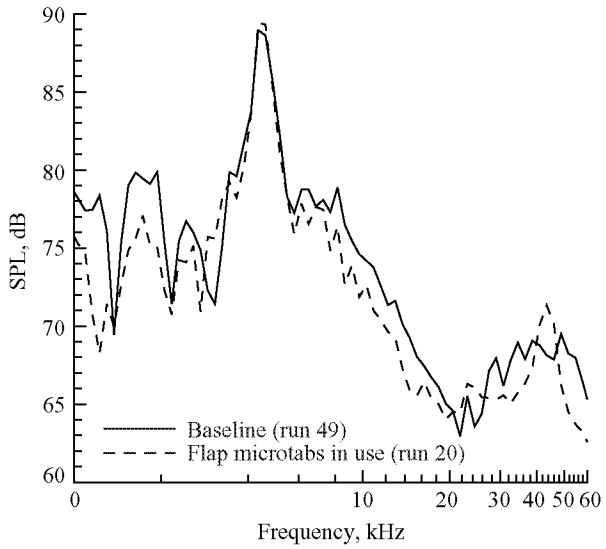

Figure 26. Integrated 1/12-octave acoustic spectra from 1998 test. $\delta_f = 20°$; Re = 7.2×10^6; $M = 0.2$.

noise reduction. For $\delta_f = 30°$, appreciable noise reduction was achieved with the microtabs placed farther inboard of the flap side edge.

More recently, relevant experiments were performed as follows: (1) a trapezoidal wing equipped with a high-lift system in the Langley 14- by 22-Foot Subsonic Tunnel (test 480) and (2) a separate 2D wing with a part-span flap in the Langley Basic Aerodynamic Research Tunnel (test 52). Results of these experiments suggest that maximum noise reduction is achieved with flap-side-edge microtabs placed two to four microtab heights inboard of the flap side edge.

Extensive evidence indicates that much of the noise associated with the flap side edge radiates from the vicinity of the trailing edge. This phenomenon is most clearly evident in the case of the low-frequency tone shown in the spectrum of figure 16 and in the localization map in figure 17. Eliminating, or at least reducing, the level of this tone is critical to obtaining any substantial noise reduction.

Serrations in wing trailing edges have been proposed by Howe as a noise-reduction technique (ref. 25). In reference 25, the proposed serrations covered the full extent of the wing's trailing edge, and the work did not investigate whether aerodynamic performance had been degraded by the use of the serrations. Flaps are part of the aircraft's high-lift system and are subject to detailed scrutiny during the flight certification process. Any noise-reduction modification must guarantee that it induces negligible degradation to the system's aerodynamic performance.

A proposed modification involved the inclusion of a short span of trailing-edge serrations near the flap side edge. Force-balance data showed less than 0.5 percent change in lift with all of the proposed noise reduction modifications. The modified side edge spanned 2 in. Figure 27 shows a photograph of the device, which we call a "noise weeder" because of an appearance similar to certain garden implements. The specific noise weeder that we tested included three full serrations and a half-tooth terminating each spanwise end of the modified section. Each full serration spanned 0.5 in., cut 0.5 in. into the unmodified edge, and extended 0.5 in. beyond the unmodified edge. With these dimensions, the sweep angle of the serration tip was slightly more than 60° and the serrations maintained the same surface area as the

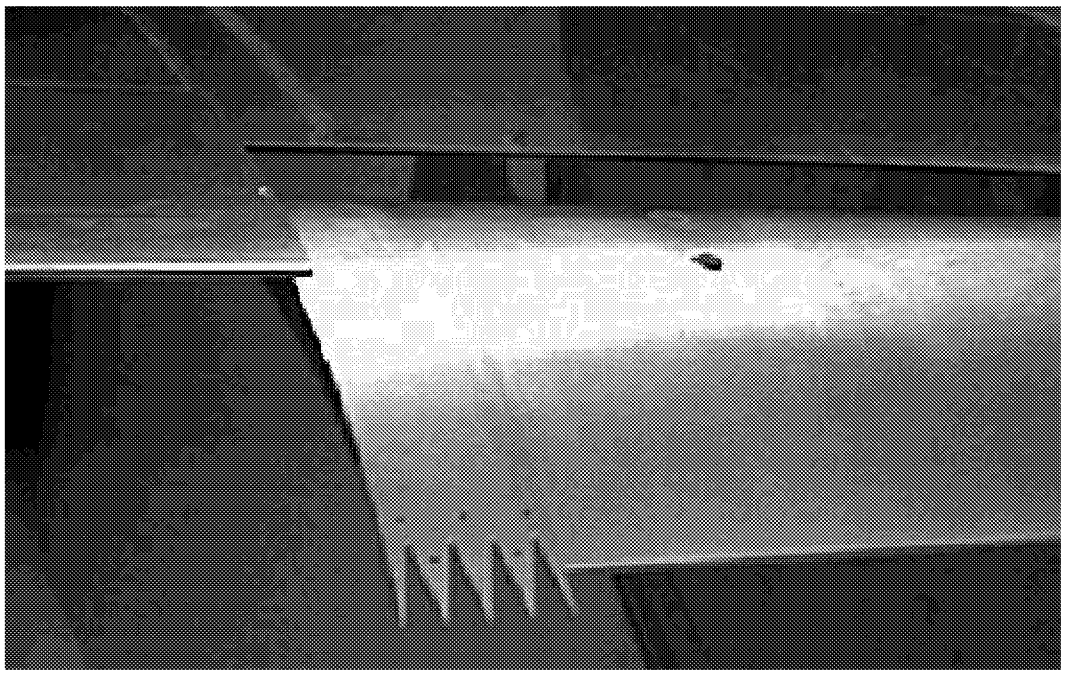

Figure 27. Noise weeder on flap side edge.

unmodified edge, i.e., regions where the serrations cut into the trailing edge were balanced by regions where the serrations extended beyond the unmodified trailing edge.

This "equivalent surface area" approach is believed to be important to maintaining aerodynamic performance. Further tests would be necessary to determine the degree to which deviations from the equivalent surface area guideline could be tolerated. Because the unmodified flap included a finite-thickness trailing edge, projecting the general contour of the airfoil profile into the extended portion of the serration was straightforward.

The serration dimensions were chosen to minimize the span over which serrations were necessary to achieve flap-side-edge noise reduction. The 2-in. span of the modification was chosen to include the path of the flap-side-edge vortex as it rolled to the suction surface near the trailing edge. This span was inferred from previous tests (for instance, see figure 6) and calculations (ref. 12). By assuming that the flow features scale with the geometry, we believe that an appropriate span for a full-scale flap, would be twice the distance from the centerline of the flap-side-edge vortex to the flap side edge at the point where the side-edge vortex passes the flap trailing edge.

Although further experimentation might reveal other successful options, the "three full teeth, two half-tooth" configuration is believed to be a good choice even for a full-scale flap. The use of the half-tooth at each spanwise end of the modified region facilitates mating the modified region with the unmodified region. The half-tooth also provides for a clean flap side edge. Variations to allow for wing sweep and other three-dimensional effects can be incorporated as well. The approximate 60° sweep angle of each serrated tip is believed to be a good choice that balances the acoustic scattering reduction effect achieved with high sweep and the practical problems associated with having numerous narrow teeth.

Figure 28 compares spectra with and without the noise weeder for the case of $\delta_f = 20°$. The low-frequency peaks are effectively removed by the noise weeder. A slight increase in noise above about 16 kHz is indicated.

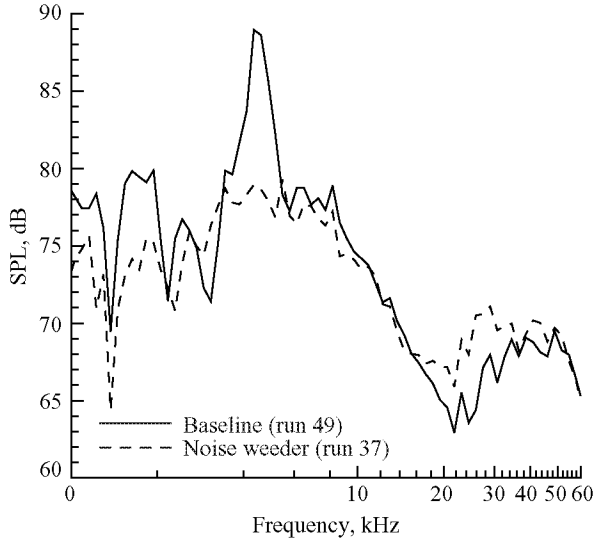

Figure 28. Integrated 1/12-octave acoustic spectra from 1998 test. $\delta_f = 20°$; Re = 7.2×10^6; $M = 0.2$.

Because of time restrictions during the 1998 test, the noise weeder modification alone was not tested with $\delta_f = 30°$. Instead, the noise weeder was tested in combination with microtabs. Figure 29 shows the integrated acoustic spectra for a baseline case and a case with the noise weeder and microtabs. In this case, microtabs were included on the main element pressure surface in the side-lap region (see fig. 30) and on the noise weeder pressure surface slightly inboard of the side edge (see fig. 31). The noise weeder

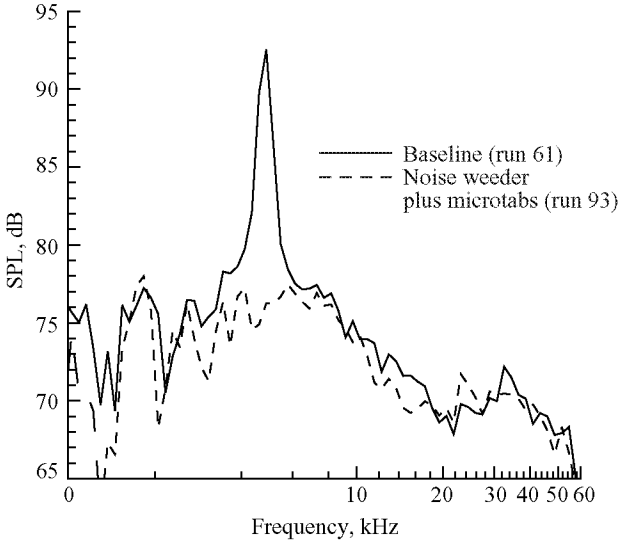

Figure 29. Integrated 1/12-octave acoustic spectra from 1998 test. $\delta_f = 30°$; Re = 7.2×10^6; $M = 0.2$.

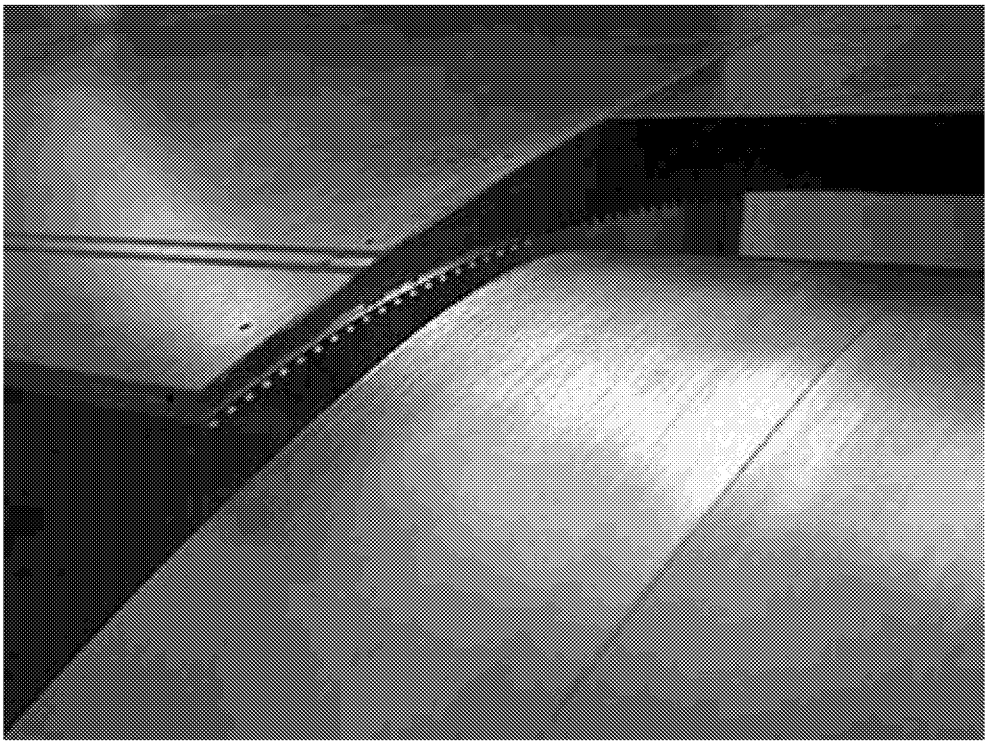

Figure 30. Microtabs on pressure surface of main element in side-lap region. View is from trailing edge of flap towards side-lap region.

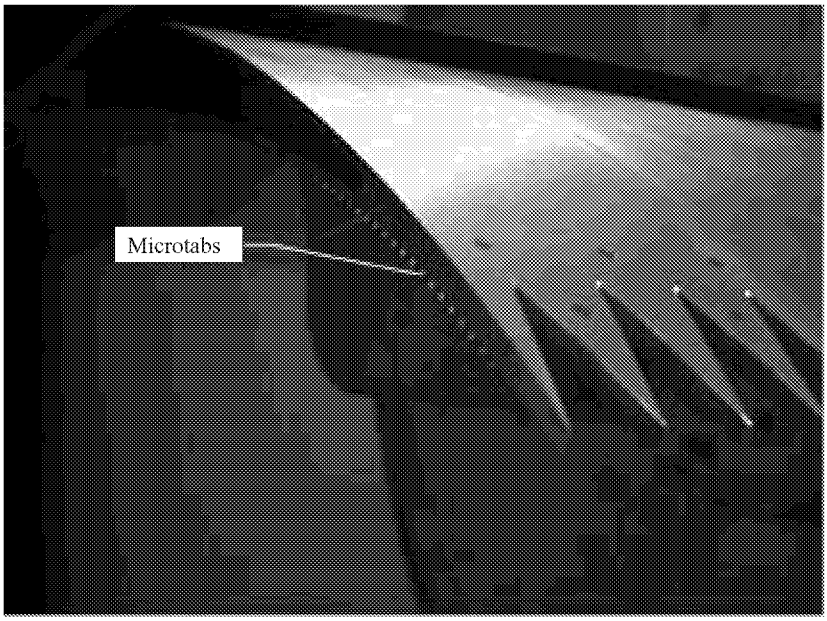

Figure 31. Microtabs on side edge of noise weeder.

essentially eliminated the low-frequency tone that existed at just under 5 kHz. In addition, some improvement in the noise was achieved in the mid-frequency range where the shear layer instabilities are important. With regard to the high-frequency noise, the data show essentially no change in the noise. Further optimization of the noise-reduction techniques could be expected to provide additional reductions.

Figures 32–36 show localization plots for run 93. Along with the noise weeder, this run used microtabs on the main element pressure surface and on the pressure surface of the flap side edge. As for the baseline case in figures 17–20, the array centroid was approximately 1 m from the flap suction surface. Except for the additional frequency of 23 041 Hz in figure 35, the frequencies are the same as those shown for the baseline case. Although the actual levels of the contours differ in each figure, the decibel range is approximately the same in all the localization plots. Comparison between the baseline case and the modified case shows how the modifications have altered the locations of the dominant noise sources.

Comparing figures 17 and 32 shows that at 4870 Hz, the modifications removed the maximum that was slightly downstream of the flap trailing edge and left a maximum slightly upstream of the flap trailing edge. A significant reduction in the maximum SPL also occurred. Spectra shown in figure 28 indicate that the presence of the noise weeder alone removed the low-frequency tone. At 9173 Hz, figure 33 shows the maximum at the flap side edge from figure 18 was reduced, leaving two maxima, one slightly upstream and one slightly downstream. A reduction in the maximum also occurred for 16312 Hz. This reduction was accompanied by the elimination of the most upstream peak in figure 19; this peak does not appear in figure 34. A localization plot at 23041 Hz (fig. 35) is included for the case with the edge modifications because the noise at this frequency was greater with the modifications than without them. The dominant noise source appeared to be at the flap side edge at about 2/3 chord. Some noise that might be considered side-lap noise developed further upstream. A minor noise source appeared slightly downstream of the trailing edge. At 36517 Hz, the localization plot in figure 36 shows a considerable reduction in side-lap noise compared to the unmodified flap side edge shown in figure 20.

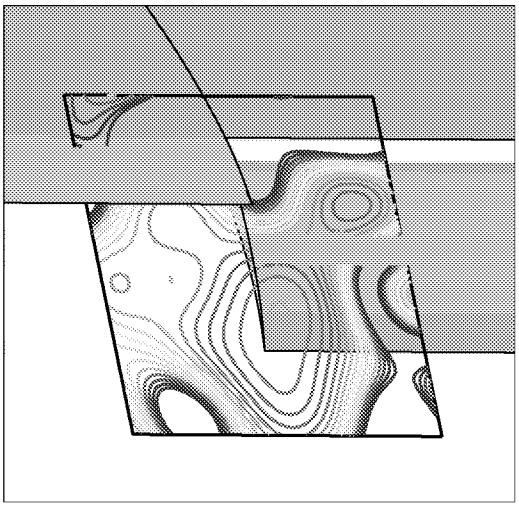

Figure 32. Localization plot for run 93 of 1998 test. f = 4870 Hz; δ_f = 30°; Re = 7.2 × 10^6; M = 0.2. Local 1/12-octave SPL peak is 71.2 dB.

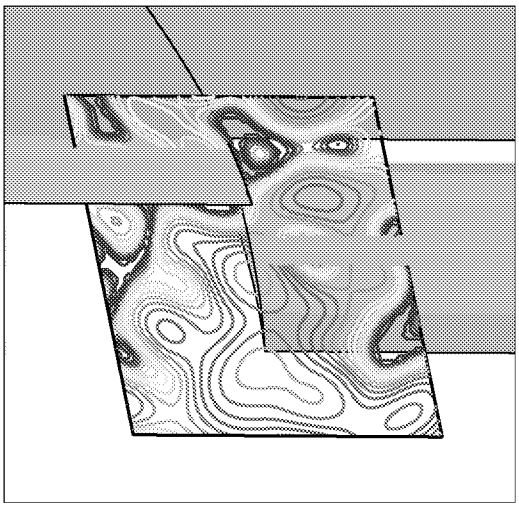

Figure 33. Localization plot for run 93 of 1998 test. f = 9173 Hz; δ_f = 30°; Re = 7.2 × 10^6; M = 0.2; local 1/12-octave SPL peak is 67.3 dB.

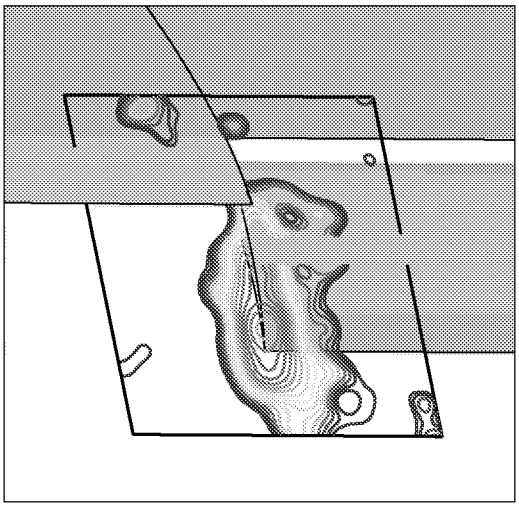

Figure 34. Localization plot for run 93 of 1998 test. f = 16312 Hz; δ_f = 30°; Re = 7.2 × 10^6; M = 0.2; local 1/12-octave SPL peak is 60.8 dB.

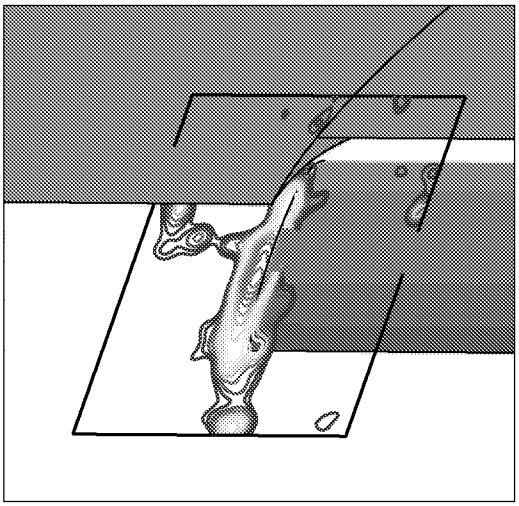

Figure 35. Localization plot for run 93 of 1998 test. f = 23 041 Hz; δ_f = 30°; Re = 7.2 × 10^6; M = 0.2; local 1/12-octave SPL peak is 61.7 dB.

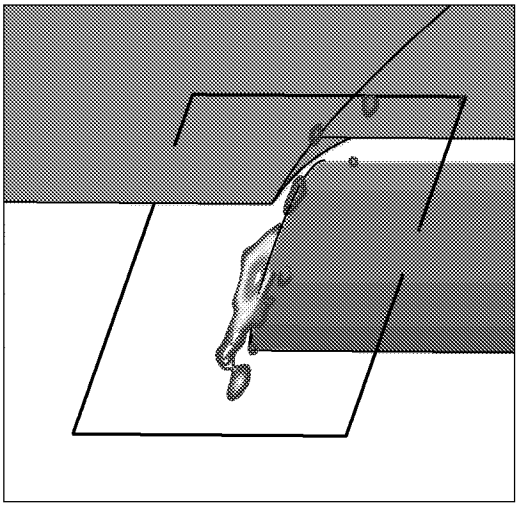

Figure 36. Localization plot for run 93 of 1998 test. f = 36 517 Hz; δ_f = 30°; Re = 7.2 × 10^6; M = 0.2; local 1/12-octave SPL peak is 63.2 dB.

These observations suggest that the noise weeder removed the low-frequency tone associated with the flap-side-edge vortex traversing the flap trailing edge. In addition, the microtabs on the pressure surface of the main element appeared to have significantly reduced the side-lap noise, and the microtabs on the flap side edge appeared to have reduced the shear layer noise. The noise weeder might have introduced some high-frequency noise (the small source downstream of the trailing edge), as was shown in the $\delta_f = 20°$ spectra of figure 28, but the $\delta_f = 30°$ spectra in figure 29 show little change in the high frequencies.

3.2. Leading-Edge Slat

3.2.1. Mean Flow

A typical static pressure distribution on the slat is shown in figure 37. For this case, the slat was deflected with $\delta_s = 30°$. Flow on the pressure side of the slat separated at the slat cusp, but reattached upstream of the trailing edge. Other experiments on a similar configuration found the reattachment was unsteady and could produce strong fluctuations in the flow field (ref. 26).

Much of the mean flow information about the slat flow field was derived from computational studies (refs. 9 and 10). The computations were three-dimensional (3D) and included the part-span flap, but not the flap nor slat brackets. Figure 38 shows streamlines superimposed on Mach contours in the region around the slat. The large recirculation region is evident in the figure. A free-shear layer developed on the edge of the recirculation zone. Fluid was accelerated through the gap at maximum speeds almost 2.5 times the free-stream velocity. Another important observation was that the slat flow field was essentially 2D, in spite of the inclusion of the part-span trailing flap. However, the presence of the slat brackets in the wind tunnel experiments most certainly introduced at least local 3D effects into the flow.

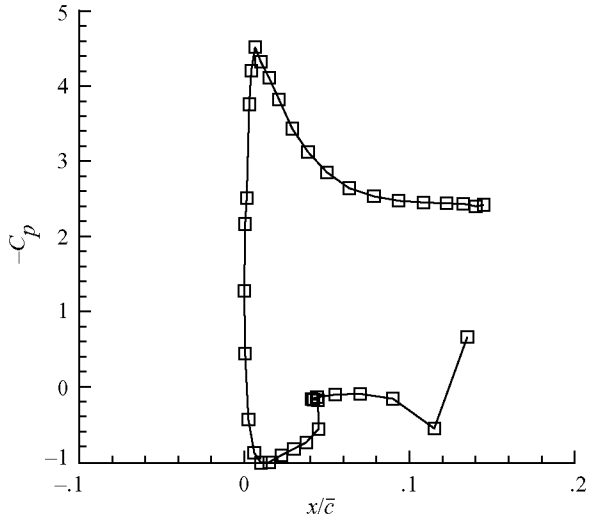

Figure 37. Pressure coefficient measured on slat centerline. $\alpha = 10°$; $\delta_f = 30°$; $\delta_s = 30°$.

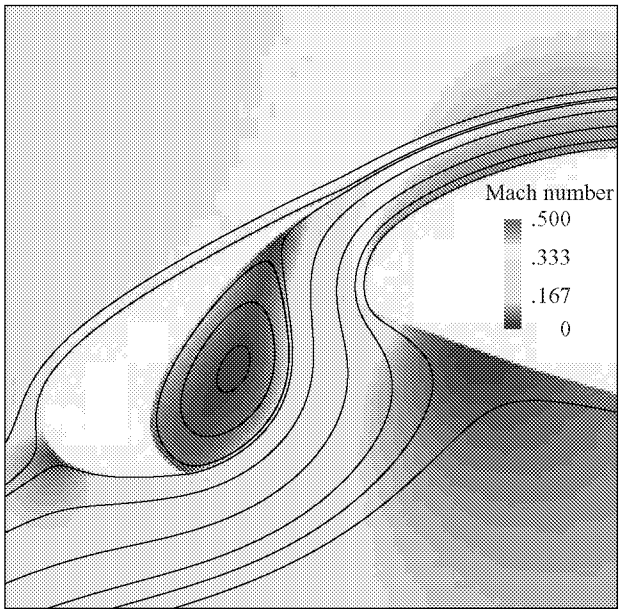

Figure 38. Streamlines superimposed on Mach contours in vicinity of slat. Spanwise location is 1 in. inboard from flap side edge. $\alpha = 10°$; $\delta_f = 30°$; $\delta_s = 30°$; $M = 0.2$.

3.2.2. Unsteady Surface Pressures

The locations of five unsteady pressure transducers used on the slat in the 1998 test are illustrated in figure 39. Figure 40 shows the spectra from transducers 1 and 5 and from a single microphone of the microphone array. The broad peak above 40 kHz in the microphone signal is probably related to the unsteady vortex shedding at the slat trailing edge, as discussed below. The surface pressure signal also appears to increase slightly in this frequency range.

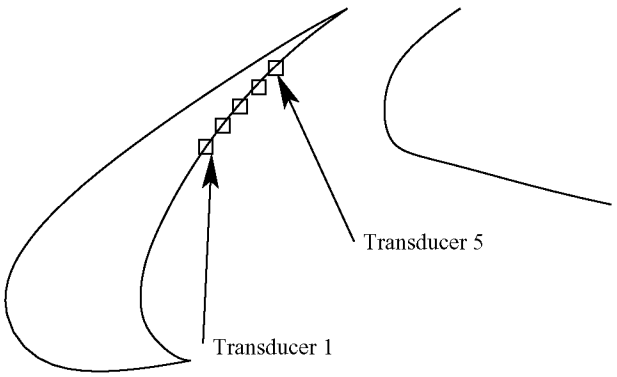

Figure 39. Schematic of five unsteady pressure transducer locations on slat.

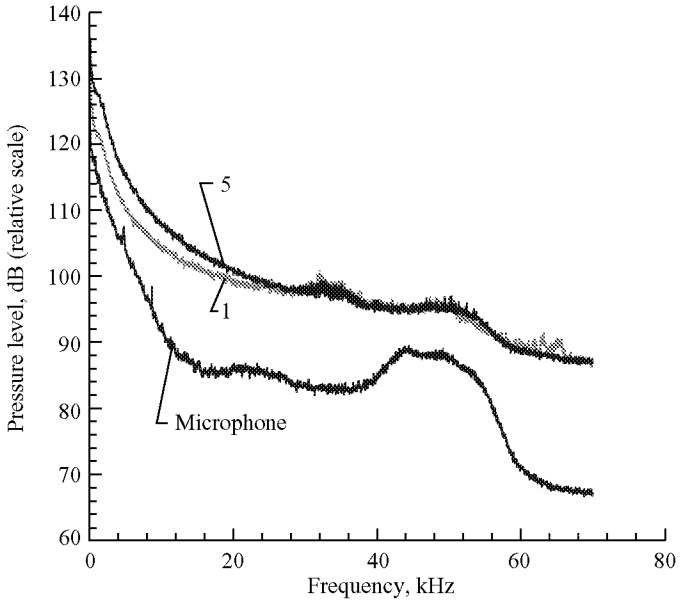

Figure 40. Signals from transducers 1 and 5 on slat, plus a microphone of the acoustic array.

3.2.3. Acoustics

During the 1998 tests, the slat noise spectra were dominated by a high-amplitude, high-frequency peak. Figure 41 shows the spectra for two slat deflections. The high-frequency peak is very clear for $\delta_s = 30°$, but is substantially reduced for the $\delta_s = 20°$ case. Khorrami et al. (ref. 10) hypothesized that vortex shedding at the slat trailing edge was responsible for the high-frequency noise. Their 2D

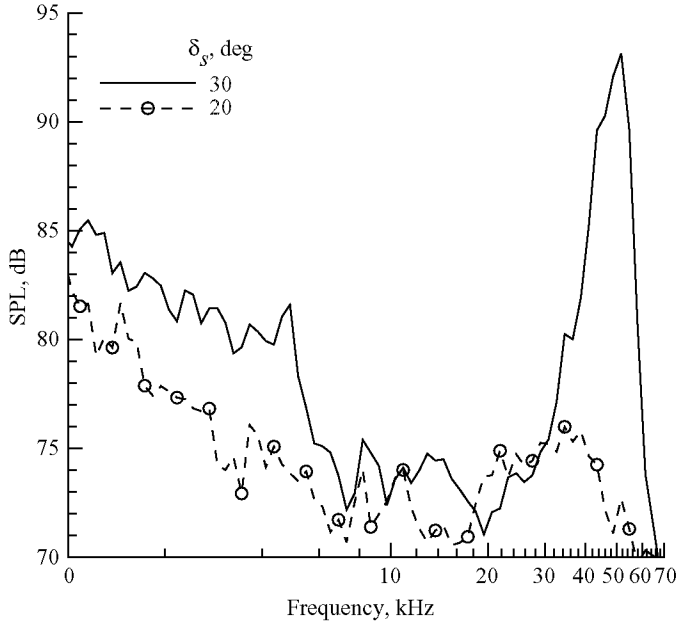

Figure 41. Integrated 1/12-octave spectra on slat. $\alpha = 10°$; Re = 7.2×10^6; $M = 0.2$.

unsteady calculations support this theory. With this unsteady data as input, the acoustic analogy calculations of Singer, Lockard, and Brentner (ref. 8) demonstrated that the vortex shedding produced sufficient noise to explain the peak and that the directivity of the computed acoustic signal was consistent with individual microphone data from the experiment.

Storms et al. (ref. 27) noted a similar strong sensitivity to slat deflection in experiments on a different high-lift system. They attributed the difference to a laminar turbulent transition on the suction surface of the slat. At the lower slat deflections, a laminar separation bubble had a turbulent reattachment, while for the higher slat deflections, no separation bubble was expected and the flow remained laminar. On the suction surface, a laminar boundary layer would have been more prone than a turbulent one to vortex shedding at the trailing edge and hence could account for the production of the high-frequency tone at the higher slat deflections. However, the current study was conducted at a variety of significantly higher Reynolds numbers. Figure 42 shows the spectra for four different Reynolds numbers with $M = 0.2$ and $\delta_s = 30°$. The loud tone shows some variability for the two lower Reynolds numbers, but is remarkably similar for the two higher Reynolds numbers. Therefore, a transition effect would not likely account for the difference between the two slat deflections.

Because the geometry of the 20° slat deflection differed from that of the 30° slat deflection, a resonance mechanism that might be involved in the slat tone noise for the 30° slat deflection probably would not be applicable to the case with the 20° slat deflection. Such resonances were considered as potentially amplifying the noise generated by the vortex shedding. No simple resonance theory has yet been developed.

The 1999 tests were designed to confirm the source of the high-frequency peak and to explore a method for reducing the low-frequency noise. To aid in the investigations, an additional small-aperture

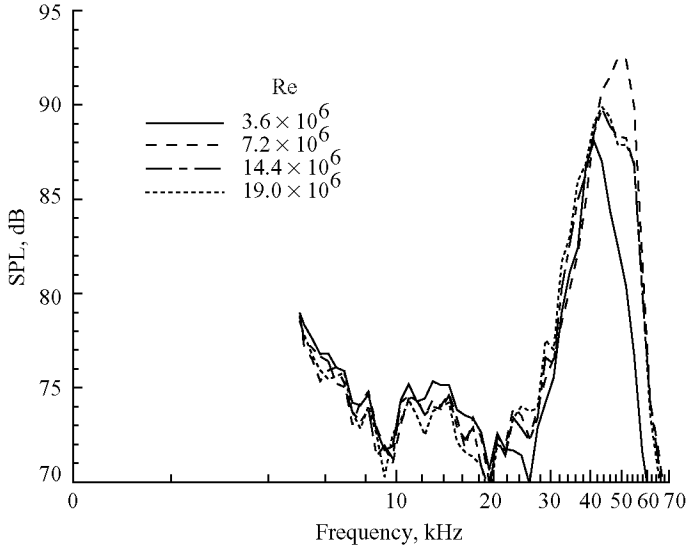

Figure 42. Integrated 1/12-octave spectra on slat. $\alpha = 10°$; $\delta_s = 30°$; $M = 0.2$.

array was used in conjunction with the large-aperture array. The small-aperture array was designed to focus more distinctly on high-frequency noise emanating from the vicinity of the slat. The array centroid was approximately 1 m from the pressure surface, slightly upstream of the slat leading edge and biased off the wind tunnel centerline. An acoustic localization map is shown in figure 43. In contrast, the large-aperture array had its centroid slightly upstream of the quarter chord portion of the main element.

Although the small-aperture array was designed primarily to collect high-frequency data, for many cases small-aperture array data were collected in sufficiently long segments for the data to be processed to lower frequencies. Baseline and modified wing data are shown only over frequency ranges in which data were available for both cases.

3.2.4. Slat Modifications

Three modifications were made to the basic slat configuration. Two of the modifications were designed to reduce the noise emanating from the slat trailing edge; the third was designed to reduce broadband cove noise.

The first modification involved the placement of serrated tape near the trailing edge of the suction surface of the slat. Figure 44 shows the tape on the slat. Figure 45 shows a close-up view that indicates roughly the dimensions involved. The intended purpose of the tape was to thicken the boundary layer on the slat and thereby eliminate or reduce the vortex shedding that was so dominant on the baseline model. A comparison of the microphone array spectra, with and without the tape, is shown in figure 46. The use of the serrated tape reduced the high-frequency peak by approximately 6 to 7 dB.

The second slat modification replaced the trailing edge of the slat with a sharper trailing edge. Rather than having a trailing-edge thickness of approximately 0.020 in., the nominal trailing-edge thickness was reduced to approximately 0.010 in. Unfortunately, this slat trailing edge was not uniform across the span.

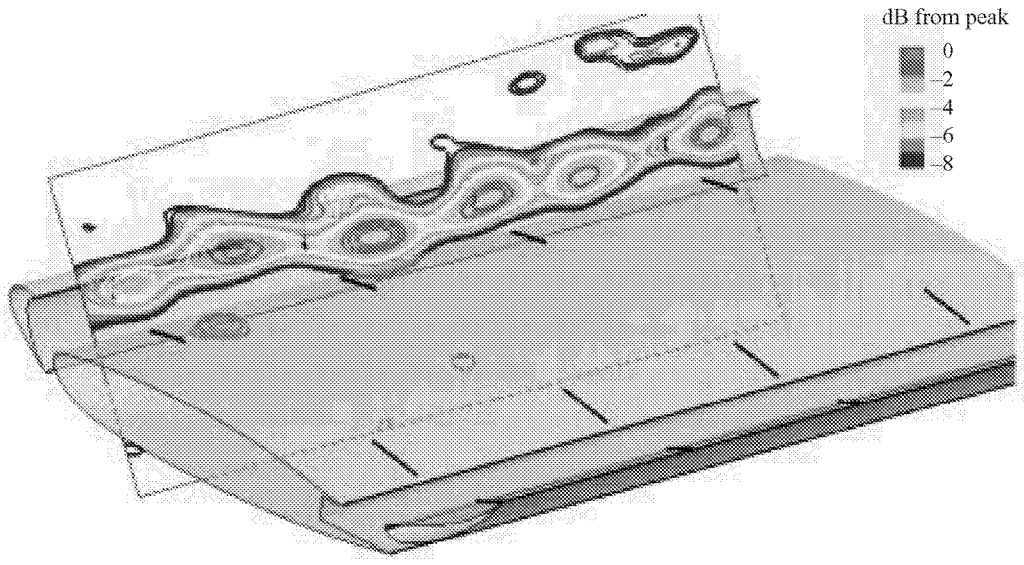

Figure 43. Localization plot from small-aperture acoustic array for run 38 of 1999 test. f = 48 697 Hz; $\alpha = 6°$; $\delta_s = 30°$; Re = 7.2×10^6; $M = 0.2$; local 1/12-octave SPL peak is 80.3 dB.

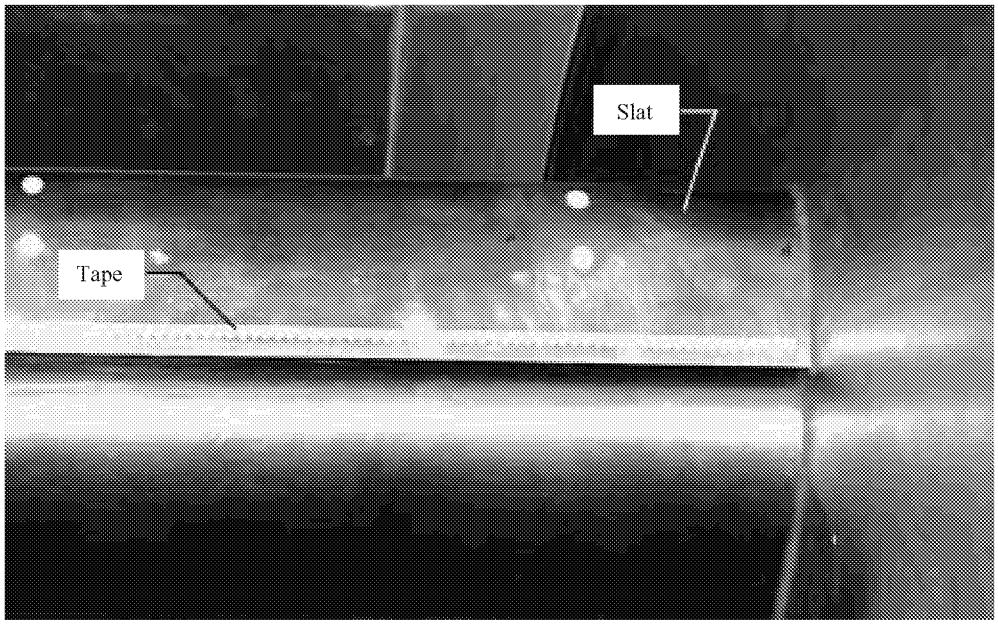

Figure 44. Serrated tape on suction surface of slat. Because model is inverted, view is from floor looking towards tunnel ceiling.

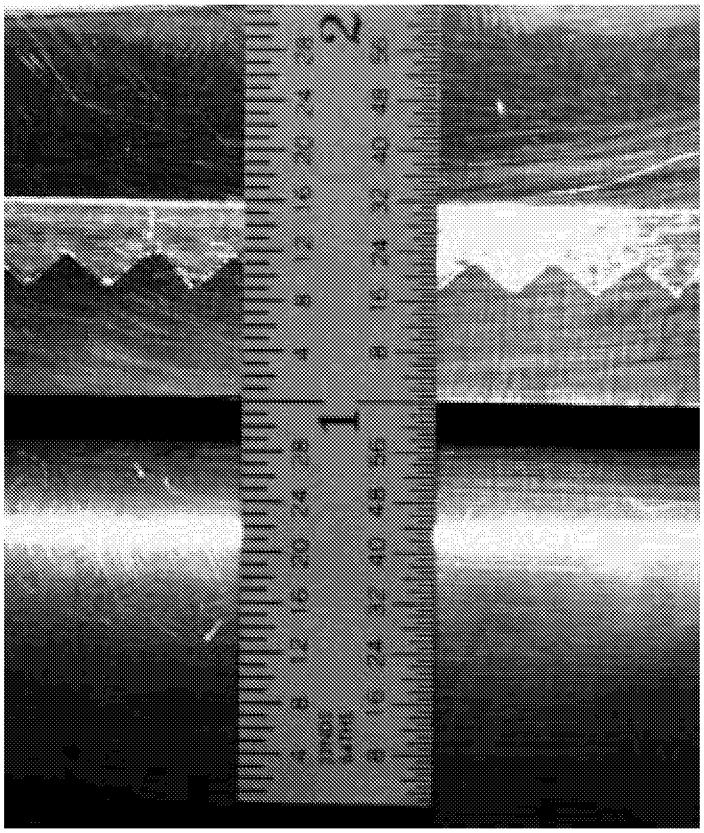

Figure 45. Close-up view of serrated tape on suction surface of slat.

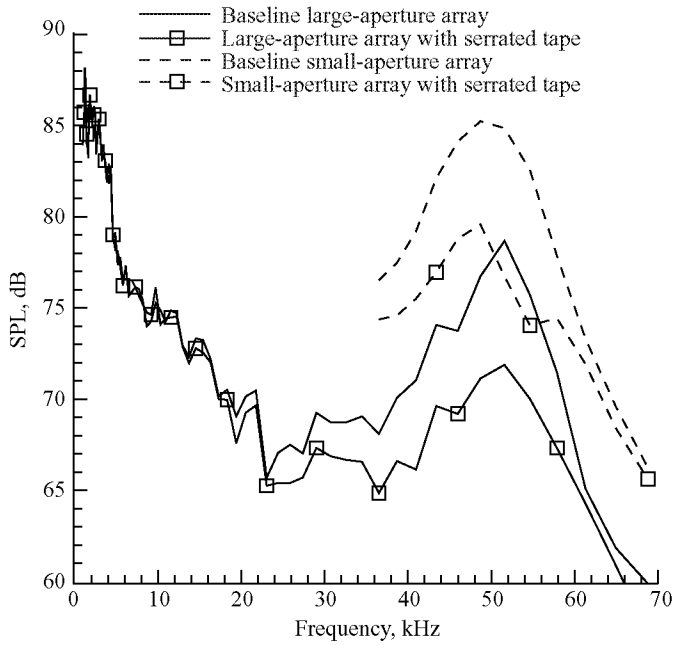

Figure 46. Integrated 1/12-octave spectra on slat. $\alpha = 6°$; $\delta_s = 30°$; Re = 7.2×10^6; $M = 0.2$.

A tone at approximately 14 kHz developed at a number of conditions with the thinner slat trailing edge. Although the exact cause of the tone is not yet understood, figure 47 is a localization plot at 14 kHz that suggests the source of this tone is near center-span of the slat. Therefore, this tone does not appear to be associated with bracket noise, but may be associated with the nonuniform trailing-edge thickness.

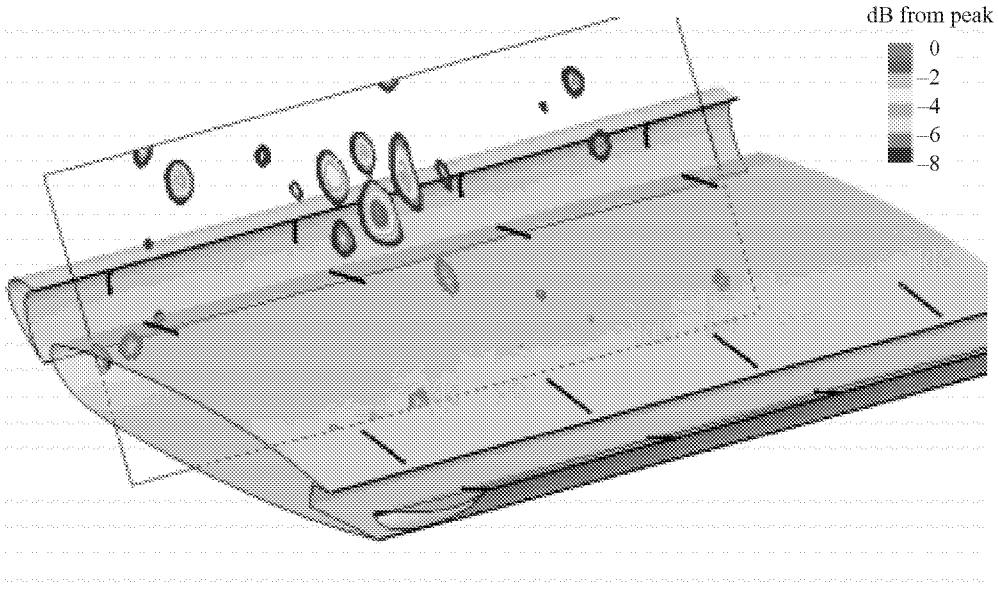

Figure 47. Localization plot from large-aperture acoustic array for run 98 of 1999 test; thin trailing edge; $f = 14538$ Hz; $\alpha = 6°$; $\delta_s = 30°$; Re = 7.2×10^6; $M = 0.2$; local 1/12-octave SPL peak is 81.1 dB.

However, the tone does not appear for cases with Re = 14.4×10^6. Although a deeper understanding of the 14 kHz tone is desirable, the higher Reynolds number more closely approximates the Reynolds number range of a commercial aircraft on approach. Figure 48 shows that at this higher Reynolds number the noise is greatly reduced from the baseline case. The reduction is almost 10 dB in the frequency range associated with the vortex shedding noise.

The above results indicate that certain slat modifications dramatically reduced the noise produced in the vicinity of the 50 kHz tone that was observed in the baseline case. The slat modifications that resulted in such reductions were designed to either increase the slat-trailing-edge boundary-layer thickness or decrease the slat-trailing-edge thickness. This experimental observation strongly supports the computational conclusions in references 8 and 10 that vortex shedding was responsible for the 50 kHz tone.

The third slat modification was designed to reduce the lower frequency broadband noise. This modification was similar to the partial slat coverings used by Dobrzynski et al. (ref. 3) and shown in reference 28. However, instead of a partial slat covering, a closed surface filler was inserted into the slat cove. Previous experiments that employed slat-cove fillers had used the separation streamline to define the filler geometry (refs. 29 and 30). However, the use of such a filler geometry resulted in the formation of a large separation bubble on the aft portion of the filler and the generation of a significant amount of high-frequency noise.

In the current study, the design philosophy was to fill the cove region in such a way that the gap between the slat and the main element was a smoothly converging duct. A cross section of the slat and the filler is shown in figure 49.

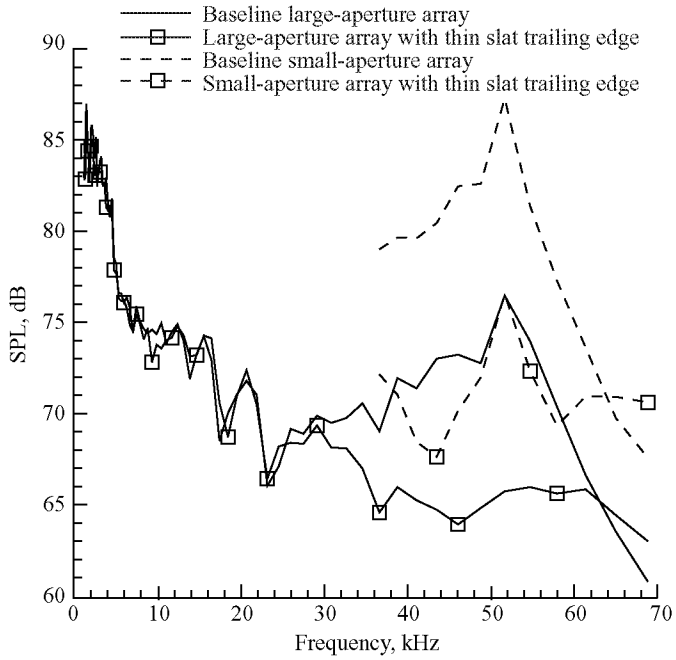

Figure 48. Integrated 1/12-octave spectra on slat. $\alpha = 6°$; $\delta_s = 30°$; Re = 14.4×10^6; $M = 0.2$.

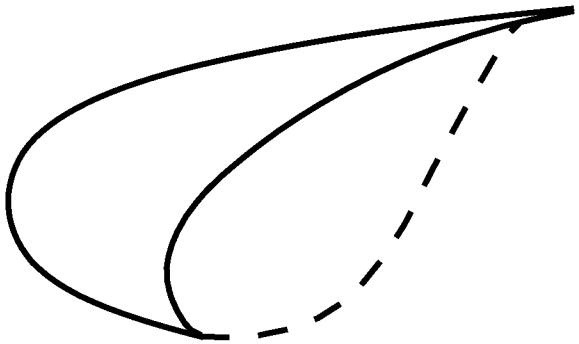

Figure 49. Schematic of slat (solid line) with slat-cove filler (dashed line).

The slat-cove filler was used only with the thinner slat trailing edge. This configuration was expected to be the quietest. The spectra obtained are compared with a baseline case in figure 50. The noise reduction achieved with the slat filler was highly dependent on frequency. A reduction of approximately 10 dB was observed over a significant portion of the 0-20 kHz range.

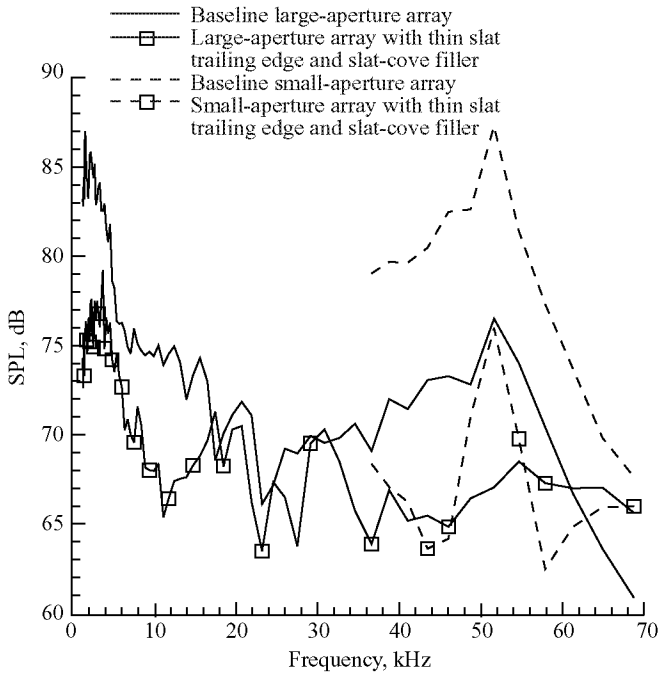

Figure 50. Integrated 1/12-octave spectra on slat. $\alpha = 6°$; $\delta_s = 30°$; Re = 14.4×10^6; $M = 0.2$.

4. Concluding Remarks

This report describes details of experimental airframe noise investigations performed in the Langley Low-Turbulence Pressure Tunnel. Reynolds numbers ranging from 3.6×10^6 to 19.2×10^6 were explored. In the various tests, steady and unsteady surface pressure data were obtained in addition to phased microphone array data. This work focused on noise emanating from the flap and slat portions of a high-lift wing.

The flap side edge produces a complicated flow comprising multiple vortices that propagate downstream and merge. When the data were evaluated in conjunction with associated numerical simulations, four primary mechanisms were suggested for the generation of noise from the flap side edge. Flap-side-edge modifications that interfered with these mechanisms were shown to reduce the radiated noise without incurring significant aerodynamic penalties.

Noise radiation from the slat still is not well characterized. One mechanism is associated with vortex shedding from the slat trailing edge. Other mechanisms probably are associated with the separated flow in the slat cove, but these mechanisms are not yet clearly understood. Modifications to the slat trailing edge can essentially eliminate the noise from the vortex shedding. A slat-cove filler significantly reduced the low-frequency noise by essentially eliminating the separation zone in the slat cove.

References

1. Davy, H.; and Remy, R.: Airframe Noise Characteristics on a 1/11 Scale Airbus Model. AIAA-98-2335, 1998.

2. Hayes, J. A.; Horne, W. C.; Soderman, P. T.; and Bent, P. H.: Airframe Noise Characteristics of a 4.7% Scale DC-10 Model. AIAA-97-1594, 1997.

3. Dobrzynski, W.; Nagakura, K.; Gehlhar, B.; and Buschbaum, A.: Airframe Noise Studies on Wings With Deployed High-Lift Devices. AIAA-98-2337, 1998.

4. Macaraeg, M. G.: Fundamental Investigations of Airframe Noise. AIAA-98-2224, 1998.

5. Meadows, K. R.; Brooks, T. F.; Gerhold, C. H.; Humphreys, W. M. Jr.; and Hunter, W. W.: Acoustic and Unsteady Surface Pressure Measurements of a Main Element-Flap Configuration. AIAA-97-1595, 1997.

6. Radeztsky, R. H.; Singer, B. A.; and Khorrami, M. R.: Detailed Measurements of a Flap Side-Edge Flow Field. AIAA-98-700, 1998.

7. Brooks, T. F.; and Humphreys, W. M. Jr.: Flap Edge Aeroacoustic Measurments and Predictions. AIAA-2000-1975, 2000.

8. Singer, B. A.; Lockard, D. P.; and Brentner, K. S.: Computational Acoustic Analysis of Slat Trailing-Edge Flow. *AIAA J.*, vol. 38, no. 9, Sept. 2000, pp. 1558–1564.

9. Berkman, M. E.; Khorrami, M. R.; Choudhari, M.; and Sadowski, S. S.: Investigation of High-Lift Flow Field of an Energy Efficient Transport Wing. AIAA-99-0926, 1999.

10. Khorrami, M. R.; Berkman, M. E.; Choudhari, M.; Singer, B. A.; Lockard, D. P.; and Brentner, K. S.: Unsteady Flow Computations of a Slat With a Blunt Trailing Edge. AIAA-99-1805, 1999.

11. McGhee, R. J.; Beasley, W. D.; and Foster, J. M.: *Recent Modifications and Calibration of the Langley Low-Turbulence-Pressure Tunnel.* NASA TP-2328, 1984.

12. Morgan, H. L.: *Model Geometry Description and Pressure Distribution Data From Tests of EET High-Lift Research Model Equipped With Full-Span Slat and Part-Span Flaps.* NASA TM-80048, 1979.

13. Lin, J. C.; and Dominik, C. J.: Parametric Investigation of High-Lift Airfoil at High Reynolds Numbers. *J. Aircr.*, vol. 33, no. 4, 1997, pp. 485–491.

14. Underbrink, J. R.; and Dougherty, R. P.: Array Design for Non-Intrusive Measurements of Noise Sources. *Proceedings of NOISECON 96*, J. D. Chalupnik, S. E. Marshall, and R. C. Klein, eds., Institute of Noise Control Engineering, Washington, DC, 1996.

15. Dougherty, R. P.: *Spiral-Shaped Array for Broadband Imaging.* U.S. Patent No. 5,838,284, 1998.

16. Mosher, M.: Phased Arrays for Aeroacoustic Testing—Theoretical Development. AIAA-96-1713, 1996.

17. Mosher, M.; Watts, M. E.; Jaeger, S. M.; and Jovic, S.: Calibration of Microphone Arrays for Phased Array Processing. AIAA-97-1678, 1997.

18. Radeztsky, R. H.; Singer, B.S.; and Khorrami, M. R.: Detailed Measurements of a Flap Side-Edge Flow Field. AIAA-98-0700, 1998.

19. Khorrami, M. R.; Singer, B. A.; and Radeztsky, J.: Reynolds-Averaged Navier-Stokes Computations of Flap-Side-Edge Flowfield. *AIAA J.,* vol. 37, no. 1, 1999, pp. 14–22.

20. Storms, B. L.; Takahashi, T. T.; and Ross, J. C.: *Aerodynamic Influence of a Finite-Span Flap on a Simple Wing*. SAE Paper No. 951977, 1995.

21. Khorrami, M. R.; and Singer, B. A.: Stability Analysis for Noise-Source Modeling of a Part-Span Flap. AIAA-98-2225, 1998.

22. Streett, C. L.: Numerical Simulation of Fluctuations Leading to Noise in a Flap-Edge Flowfield. AIAA-98-0628, 1998.

23. Streett, C. L.: Numerical Simulations of a Flap-Edge Flowfield. AIAA-98-2226, 1998.

24. Khorrami, M. R.; and Singer, B. A.: Stability Analysis for Noise-Source Modeling of a Part-Span Flap. *AIAA J.*, vol. 37, no. 10, 1999, p. 1206.

25. Howe, M. S.: Aerodynamic Noise of a Serrated Trailing Edge. *J. Fluids & Struct.*, vol. 5, 1991, pp. 33–45.

26. McGinley, C. B.; Anders, J. B.; and Spaid, F. W.: Measurements of Reynolds Stress Profiles on a High-Lift Airfoil. AIAA-98-2620, 1998.

27. Storms, B.; Hayes, J.; Moriarty, P. J.; and Ross, J.: Aeroacoustic Measurements of Slat Noise on the Three-Dimensional High-Lift System. AIAA-99-1957, 1999.

28. Heller, H. H.: DLR's Involvement in European Aviation Noise Research on Fixed and Rotary Wing Aircraft—A (Roughly) Five Year Retrospective. 5th AIAA/CEAS Aeroacoustics Conference Keynote Lecture, AIAA, Reston, VA, 1999.

29. Moriarty, P.: Unsteady Measurements Near a Leading-Edge Slat. *3rd Airframe Noise Workshop*, R. Sen, ed., NASA AST Program, 1998.

30. Storms, B.; Hayes, J.; and Ross, J.: Aeroacoustic Measurements of Slat Noise on a Three-Dimensional High-Lift System. *3rd Airframe Noise Workshop*, R. Sen, ed., NASA AST Program, 1998.

REPORT DOCUMENTATION PAGE

Form Approved
OMB No. 0704-0188

1. AGENCY USE ONLY *(Leave blank)*	2. REPORT DATE	3. REPORT TYPE AND DATES COVERED
	February 2002	Technical Memorandum

4. TITLE AND SUBTITLE
Aeroacoustic Experiments in the NASA Langley Low-Turbulence Pressure Tunnel

5. FUNDING NUMBERS
WU 706-81-13-02

6. AUTHOR(S)
Meelan M. Choudhari, David P. Lockard, Michele G. Macaraeg, Bart A. Singer, Craig L. Streett, Guy R. Neubert, Robert W. Stoker, James R. Underbrink, Mert E. Berkman, Mehdi R. Khorrami, and Shelly S. Sadowski

7. PERFORMING ORGANIZATION NAME(S) AND ADDRESS(ES)
NASA Langley Research Center
Hampton, VA 23681-2199

8. PERFORMING ORGANIZATION REPORT NUMBER
L-18131

9. SPONSORING/MONITORING AGENCY NAME(S) AND ADDRESS(ES)
National Aeronautics and Space Administration
Washington, DC 20546-0001

10. SPONSORING/MONITORING AGENCY REPORT NUMBER
NASA/TM-2002-211432

11. SUPPLEMENTARY NOTES
Choudhari, Lockard, Macaraeg, Singer, and Streett: Langley Research Center, Hampton, VA; Neubert, Stoker, and Underbrink: Boeing Commercial Aircraft, Seattle, WA; Berkman, Khorrami, and Sadowski: High Technology Corporation, Hampton, VA.

12a. DISTRIBUTION/AVAILABILITY STATEMENT
Unclassified–Unlimited
Subject Category 71 Distribution: Nonstandard
Availability: NASA CASI (301) 621-0390

12b. DISTRIBUTION CODE

13. ABSTRACT ***(Maximum 200 words)***
A phased microphone array was used in the NASA Langley Low-Turbulence Pressure Tunnel to obtain acoustic data radiating from high-lift wing configurations. The data included noise localization plots and acoustic spectra. The tests were performed at Reynolds numbers based on the cruise-wing chord, ranging from 3.6×10^6 to 19.2×10^6. The effects of Reynolds number were small and monotonic for Reynolds numbers above 7.2×10^6.

14. SUBJECT TERMS
Aeroacoustic noise; Flap noise; Slat noise; Flap-edge noise; Flap-side-edge noise; Airframe noise; High lift; Acoustic array

15. NUMBER OF PAGES
46

16. PRICE CODE
A03

17. SECURITY CLASSIFICATION OF REPORT	18. SECURITY CLASSIFICATION OF THIS PAGE	19. SECURITY CLASSIFICATION OF ABSTRACT	20. LIMITATION OF ABSTRACT
Unclassified	Unclassified	Unclassified	UL

NSN 7540-01-280-5500

Standard Form 298 (Rev. 2-89)
Prescribed by ANSI Std. Z39-18
298-102